A large thermal energy reservoir in the nascent intracluster medium at a redshift of 4.3

Dazhi Zhou[1*], Scott Chapman[2,1,3], Manuel Aravena[4,5],
Pablo Araya-Araya[6], Melanie Archipley[7,8], Jared Cathey[9],
Roger Deane[10,11], Luca Di Mascolo[12,13], Raphael Gobat[14],
Thomas Greve[15,16], Ryley Hill[1], Seonwoo Kim[17],
Kedar Phadke[17,18,19], Vismaya Pillai[1], Ana Posses[20],
Christian Reichardt[21], Manuel Solimano[4,5], Justin Spilker[20],
Nikolaus Sulzenauer[22], Veronica Dike[17], Joaquin Vieira[17,18,23],
David Vizgan[17], George Wang[1], Axel Weiß[22]

[1*]Department of Physics and Astronomy, University of British
Columbia, 6225 Agricultural Rd., Vancouver, V6T 1Z1, Canada.
[2]Department of Physics and Atmospheric Science, Dalhousie University,
Canada.
[3]National Research Council, Herzberg Astronomy and Astrophysics,
Canada.
[4]Instituto de Estudios Astrofícos, Facultad de Ingeniería y Ciencias,
Universidad Diego Portales, Av. Ejército 441, Santiago, Chile.
[5]Millenium Nucleus for Galaxies (MINGAL).
[6]Departamento de Astronomia, Instituto de Astronomia, Geofísica e
Ciências Atmosféricas, Universidade de São Paulo Rua do Matão 1226,
Cidade Universitária, 05508-900, São Paulo, SP, Brazil.
[7]Department of Astronomy and Astrophysics, University of Chicago,
5640 South Ellis Avenue, Chicago, IL, 60637, USA.
[8]Kavli Institute for Cosmological Physics, University of Chicago, 5640
South Ellis Avenue, Chicago, IL, 60637, USA.
[9]Department of Astronomy, University of Florida, Gainesville, FL 32611, USA.
[10]Wits Centre for Astrophysics, School of Physics, University of the
Witwatersrand, 1 Jan Smuts Avenue, 2000, Johannesburg, South Africa.
[11]Department of Physics, University of Pretoria, Hatfield, Pretoria
0028, South Africa.

1

[12]Kapteyn Astronomical Institute, University of Groningen, Landleven 12, 9747 AD, Groningen, The Netherlands.

[13]Université Côte d'Azur, Observatoire de la Côte d'Azur, CNRS, Laboratoire, Lagrange, France.

[14]Instituto de Física, Pontificia Universidad Católica de Valparaíso, Casilla 4059, Valparaíso, Chile.

[15]Cosmic Dawn Center (DAWN), Denmark.

[16]DTU Space, Technical University of Denmark, Elektrovej 327, DK-2800 Kgs. Lyngby, Denmark.

[17]Department of Astronomy, University of Illinois, 1002 West Green St., Urbana, IL 61801, USA.

[18]Center for AstroPhysical Surveys, National Center for Supercomputing Applications, 1205 West Clark Street, Urbana, IL 61801, USA.

[19]NSF-Simons AI Institute for the Sky (SkAI), 172 E. Chestnut St., Chicago, IL 60611, USA.

[20]Department of Physics and Astronomy and George P. and Cynthia Woods Mitchell Institute for Fundamental Physics and Astronomy, Texas A&M University, 4242 TAMU, College Station, TX 77843-4242, USA.

[21]School of Physics, University of Melbourne, Parkville, VIC 3010, Australia.

[22]Max-Planck-Institut für Radioastronomie, Auf dem Hügel 69, 53121, Bonn, Germany.

[23]Department of Physics, University of Illinois, 1110 West Green St., Urbana, IL 61801, USA.

*Corresponding author(s). E-mail(s): dzhou.astro@gmail.com;

Abstract

Most baryons in present-day galaxy clusters exist as hot gas ($\gtrsim 10^7$ K), forming the intracluster medium (ICM) [1]. Cosmological simulations predict that the mass and temperature of the ICM rapidly decrease with increasing cosmological redshift, as intracluster gas in younger clusters is still accumulating and being heated [2–4]. The thermal Sunyaev-Zeldovich (tSZ) effect arises when cosmic microwave background (CMB) photons are scattered to higher energies through interactions with energetic electrons in hot ICM, leaving a localized decrement in the CMB at a long wavelength [5, 6]. The depth of this decrement is a measure of the thermal energy and pressure of the gas [7]. To date, the effect has been detected in only three systems at or above $z \sim 2$, when the Universe was 4 billion years old, making the time and mechanism of ICM assembly uncertain [8–10]. Here, we report observations of this effect in the protocluster SPT2349−56 with Atacama Large Millimeter/submillimeter Array (ALMA). SPT2349−56 contains

2

a large molecular gas reservoir, with at least 30 dusty star-forming galaxies (DSFGs) and three radio-loud active galactic nuclei (AGN) in a 100-kpc region at $z = 4.3$, corresponding to 1.4 billion years after the Big Bang [11–14]. The observed tSZ signal implies a thermal energy of $\sim 10^{61}$ **erg**, exceeding the possible energy of a virialized ICM by an order of magnitude. Contrary to current theoretical expectations [3, 4, 15], the strong tSZ decrement in SPT2349−56 demonstrates that substantial heating can occur and deposit a large amount of thermal energy within growing galaxy clusters, overheating the nascent ICM in unrelaxed structures, two billion years before the first mature clusters emerged at $z \sim 2$.

SPT2349−56 was selected as the brightest protocluster candidate from the 2,500 deg^2 South Pole Telescope survey [16, 17]. It is an active protocluster with a massive dark matter halo ($\sim 10^{13} M_\odot$) and a star-formation rate (SFR) of $\sim 5,000 M_\odot/\text{yr}$ within the central 100 kpc [11, 12]. At least three radio-loud active galactic nuclei (AGN) and 30 dusty star-forming galaxies (DSFGs) are spectroscopically confirmed to reside in its core region [11–13, Chapman et al. in prep], which may provide substantial energy injection into its potential nascent intracluster medium (ICM) [13, 18–29]. A large molecular gas reservoir has been detected in SPT2349−56 through low-resolution observations by the Atacama Compact Array (ACA) [14], which might represent the cooler component of a proto-ICM, making it an ideal target to search for the thermal Sunyaev-Zeldovich (tSZ) signal.

We obtained deep Band-3 observations at 3 mm with the Atacama Large Millimeter/submillimeter Array (ALMA) 12-m and ACA 7-m arrays and combined them with archival data. After subtracting the dust continuum emission from DSFGs in the protocluster using a Fourier-space technique, a strong, extended decrement is present in the core region (Methods). The tSZ decrement peaks at 8.4σ in the image and 10.4σ in Fourier space, with an integrated flux density of $-157 \pm 16\,\mu$Jy. This signal directly traces inverse Compton scattering of cosmic microwave background (CMB) photons by hot ICM. We quantify the signal strength by the Compton-y parameter, defined as the fractional energy change of line-of-sight CMB photons, which is proportional to the integrated gas pressure along the line of sight [7, 15, 30]. The corresponding integrated value within the system is further defined as Compton-Y [5]. For SPT2349−56, the detected tSZ decrement corresponds to a Compton-y parameter of $(5.6 \pm 0.8) \times 10^{-6}$, or a Compton-$Y$ parameter of $(2.0 \pm 0.2) \times 10^{-6}\,\text{arcmin}^2$.

Because the tSZ effect is directly linked to the number density and temperature of hot electrons in a system, the ICM's thermal energy can be estimated [31]. From our measured Compton-Y value, we infer a total thermal energy $E_{\text{therm}} \approx 10^{61}$ erg (Methods). Historically, assuming shock waves as the primary heating source for a $10^{13} M_\odot$ protocluster at $z = 4$, Sunyaev and Zeldovich [15] originally predicted a $\sim 10^6$ K ICM, equivalent to a specific thermal energy of $\sim 10^{14}$ erg/g. To reproduce the observed decrement in this scenario, a gas mass of $5 \times 10^{13} M_\odot$ is required, five times the total mass of the system. Even assuming a fully collapsed system with an abundant ICM [$M_{\text{ICM}}/M_{\text{halo}} \lesssim 0.06$, 13], the expected decrement would be only

3

$Y \lesssim 4\times10^{-7}$ arcmin^2, corresponding to a distortion signal of $\lesssim 30\,\mu$Jy (Methods). The measured tSZ signal thus exceeds these theoretical expectations by at least a factor of five, suggesting a large thermal energy reservoir in the forming ICM of SPT2349$-$56.

A useful way to characterize the tSZ excess independent of cosmological redshift evolution is to compare it against the universal relation between cluster mass M and the Compton-Y parameter [32]. The ICM in galaxy clusters is known to evolve self-similarly over the past 10 billion years, resulting in a tight correlation between M and Y once the redshift dependence $E(z)^{2/3}$ is factored out [22, 32–36]. Although this relation accurately describes most tSZ-detected systems [9, 10, 37–41], the Compton-Y in SPT2349$-$56 exceeds it by a factor of five (Extended Data Fig. 8), implying a breakdown of the ICM self-similarity at an epoch prior to its full virialization.

Indeed, because star formation and AGN activities were more intense and the ICM was less evolved at earlier epochs, one expects an increased scatter in the $M-Y$ relation at higher redshifts [3, 4, 22, 28, 29]. To further test this hypothesis, we used the TNG-Cluster simulations, a cosmological simulation suite of 352 zoom-in galaxy clusters, to predict the redshift evolution of the mass-normalized Compton-Y (Methods). Fig. 1 shows that the mass-normalized Y from TNG-Cluster follows the self-similar prediction in the past 12 billion years, in line with current observations [37–39, 42], whereas tSZ decrement in less evolved systems are weaker than the simulation prediction [9, 10, 40, 41]. The simulated Y consistently falls below the self-similar expectation since $z \gtrsim 3$, suggesting a cooler ICM in protoclusters at these early epochs [4], in contrast to a hotter ICM inferred from our observed tSZ decrement, with a 6.4σ deviation. Although the gas temperature can be high at such an early epoch, the hot-gas fractions of these high-redshift cluster progenitors (Extended Data Fig. 10) remains too small to explain our observed thermal energy excess (Extended Data Fig. 9) [3, 4, 43, 44].

A halo mass three times larger than current observational estimates would be required for SPT2349$-$56 to match the universal $M-Y$ relation [11, 12, 45]. The inconsistency could be even amplified if one accounts for the lower hot-gas fraction at $z > 4$. To explain the measured tSZ strength without invoking an implausibly massive halo, intense *pre-heating* of the ICM must be introduced [6, 21–24, 46, 47]. While cosmological hydrodynamical simulations reproduce the global cosmic star formation history, they often under-predict the high SFRs of systems like SPT2349$-$56 [43, 48–50]. In principle, strong AGN feedback in SPT2349$-$56 could naturally provide the required energy to the nascent ICM [13, 46, 47, 51–55] (Methods). The elevated ambient gas pressure and density at $z > 4$ confine the jets, which enhances AGN heating and reduces energy loss to expansion. This confinement allows a large amount of energy stored in the over-pressurized and therefore overheated ICM, producing the strong tSZ decrement seen in SPT2349$-$56 [22, 24, 28, 29, 56–63].

How common such enormous thermal reservoirs are in nascent ICM at $z \gtrsim 4$ remains unknown. Given that SPT2349$-$56 is a unique system from a 2,500 deg^2 survey, the observed strong tSZ decrement may simply reflect its own rarity, or may serve as a clue towards a potentially unrecognized but important short-lived stage of cluster assembly [58]. Notably, the majority of hydrodynamical simulations with state-of-the-art galaxy formation models have not predicted the extreme heating

and over-pressurized hot ICM that we observe in SPT2349−56 [3, 27, 44, 64–66]. This discrepancy could point to the need for more complicated subgrid physics for AGN feedback models at high redshifts in order to match the unanticipated hot and pressurized ICM in nascent clusters [21, 66–71].
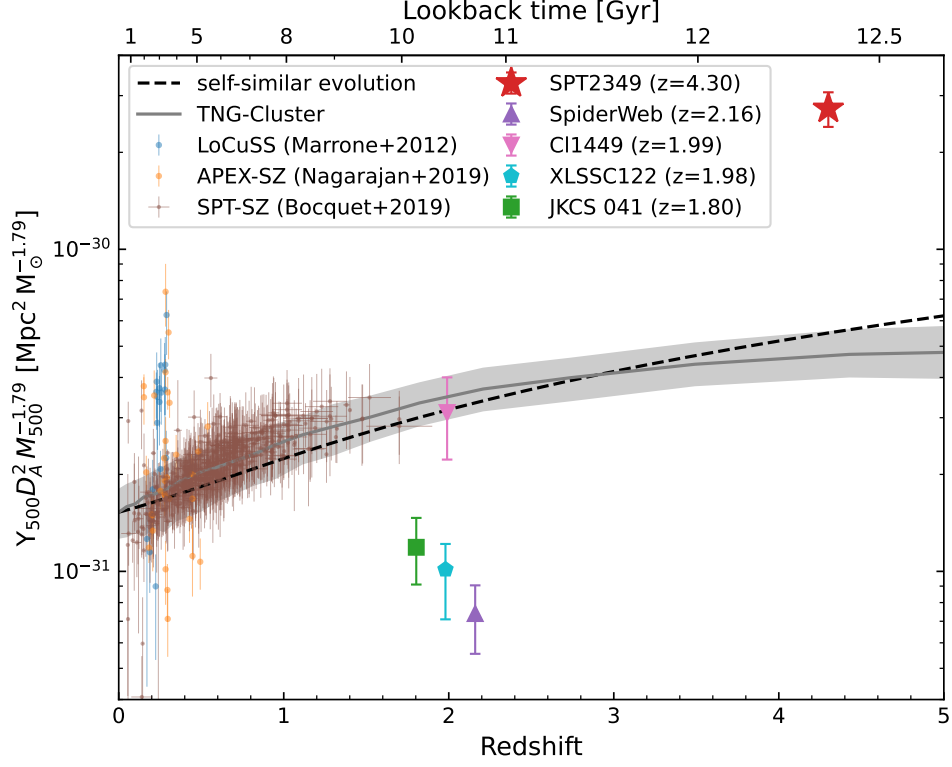
Fig. 1 Redshift evolution of the mass-normalized Compton-Y parameter. The Compton-Y_{500} is scaled by $M_{500}^{1.79}$ to remove the mass dependence, following the universal tSZ scaling relation $Y \propto M^{1.79}$[34]. The data points contain SPT-SZ [39], APEX-SZ [38], and LoCuSS [37] results, along with high-z systems detected in tSZ [9, 10, 40, 72], including SPT2349−56 at $z = 4.3$, shown as the red star. The self-similar expectation is shown as the dashed line. The solid gray line and shaded region represent the median and 68% scatter from the TNG-Cluster simulation, which has been calibrated to the local $M_{500} - Y_{500}$ relation [34]. The tSZ signal in SPT2349−56 lies 6.4σ above the predicted evolutionary tracks, in contrast to more massive systems at later epochs.
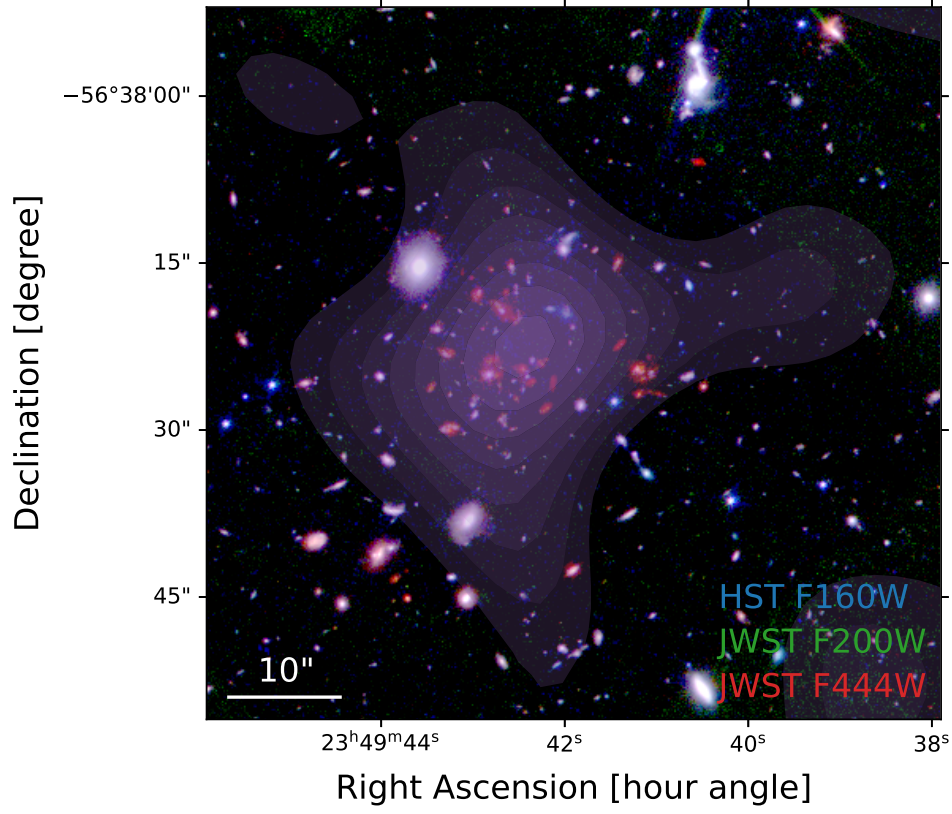
Fig. 2 RGB image of the protocluster core with tSZ decrement contours. R: JWST F444W band; G: JWST F200W band; B: HST F160W band. The tSZ signal (purple) was obtained after continuum source-subtraction in Fourier space and imaging done with short baselines ($uv < 10k\lambda$). Decrement contours are from -1σ ($8.8\,\mu$Jy) to -9σ ($79.2\,\mu$Jy) with steps of -1σ. The decrement peak (-8.4σ) is co-spatial with the kinematic center of the protocluster system. The flux density of the tSZ signal is $-157 \pm 16\mu$Jy in the image plane.

1 Methods

Throughout the paper, we used a standard Lambda Cold Dark Matter cosmological model with $H_0 = 67.7\,\mathrm{km\,s^{-1}\,Mpc^{-1}}$ and $\Omega_m = 0.31$ [73], which corresponds to a proper angular scale of $6.9\,\mathrm{kpc/arcsec}$ at $z = 4.3$. R_{200} and R_{500} are defined as the radius where the average densities are 200 and 500 times the critical density of the Universe at the source redshift. ρ_{200}, ρ_{500}, M_{200}, M_{500}, Y_{200}, and Y_{500} are the corresponding mean densities, total masses, and Compton-Y parameters within these regions, respectively.

1.1 Observations

1.1.1 ALMA observations

The ALMA and ACA Band-3 data of SPT2349$-$56 were obtained under four different programs from the ALMA Science Archive (Cycle 3: 2015.1.01543.T, PI: K. Lacaille; Cycle 5: 2017.1.00273.S, PI: S. Chapman; Cycle 9: 2022.1.00495.S, PI: J. Chen; Cycle 10: 2023.1.00124.S, PI: S. Chapman). The phase centers of these observations are similar except the Cycle 3 program, which is about 10 arcsec to the South of the pointing centers of the other programs. The total on-source exposures are 23.7 and 26.9 hours for ALMA and ACA observations, respectively. The corresponding configurations, baseline ranges, frequency ranges, correlator modes, and on-source integration times are summarized in Extended Data Table 1.

1.1.2 Ancillary data

Hubble Space Telescope (*HST*) F160W (PID: 15701, PI: S. Chapman) and *James Webb Space Telescope* (*JWST*) F200W and F444W (PID: 06669, PI: S. Chapman) images shown in Fig. 2 were retrieved from the Mikulski Archive for Space Telescopes (MAST) server. The exposure times of each filter are 8472 s (F160W), 3264 s (F200W), and 3264 s (F444W), respectively. We followed the standard reduction procedure to process the level-1 data through *HST* and *JWST* calibration pipelines (`hstcal/calwf3` and `jwst/calwebb`) within the Space Telescope Environment (`stenv`). We applied an extra de-striping step for the NIRCam images during the `stage_2` process to mitigate the influence of column stripes. The images were all reprojected and aligned to the F444W band using the python packages `reproject` and `tweakreg`. The detailed description of the *JWST* data reduction will be presented in a forthcoming paper.

1.2 ALMA data reduction

For the observations carried out before 2020, we used the standard ALMA calibration script to re-calibrate the data with the latest ALMA pipeline (`CASA` version=6.6.1). We carefully compared difference between the old and new calibrated data in their phase uncertainties, root mean square (rms) errors, and dynamical ranges of the continuum images produced from individual Execution Blocks (EBs). In general, the calibrated data obtained from the new pipeline show a $\sim 5\%$ improvement in their dynamic range. Therefore, we adopted all measurement sets calibrated by the new pipeline for consistency.

We used the observatory-calibrated measurement sets for the Cycle 9 and Cycle 10 data, which were calibrated by `CASA` 6.4.1 and `CASA` 6.6.1, respectively. According to the QA2 report from the observatory, there was some potential cloud contamination in a fraction of EBs, leading to higher phase errors. We ran the `remcloud` pipeline for better phase calibrations and inspected the improvement of the data quality. Only two EBs showed $\sim 20\%$ and $\sim 200\%$ improvements after the `remcloud` correction, which were used in this study.

Each EB was assessed by comparing the flux densities of bright sources from the `CLEAN`ed image to ensure that the calibration was consistent. The calibration was good in general,with the amplitudes of bright sources differing by $< 5\%$ at the same frequency for all EBs except two EBs, where the higher phase errors of these data introduced a loss of coherence. The high phase errors caused reduced amplitudes and elevated rms noises due to decorrelation, instead of amplitude calibration errors. In fact, the affected EBs show good agreement with other EBs after tapering, indicating that higher phase errors are dominated by the long baselines, while short baselines still keep a good coherence. Despite their worse qualities, these two EBs are still included for better uv-coverage and large-scale sensitivity. We used 'natural' weighting for all `CLEAN`ing processes in the following analysis to suppress the long-baseline contribution.

Because the accumulated data size is over a few terabytes, some data compression was needed before imaging for a higher efficiency. The latest `CASA` (version=6.7.0) was used for both preprocessing and imaging. We used the `CASA` task `mstransform` to compress all data to a common frequency and time width of 62.5MHz and 8s, respectively. This approach greatly reduces the data size and also avoids the potential bandwidth- and time-smearing effect. The phase center of each measurement set was then shifted to the pointing center of the Cycle 10 program through `phase_shift` command. Subsequently, we combined all EBs obtained from the same cycle to a single measurement set using the CASA task `concat` with `copypointing=False`. Channels with spectral lines were flagged by the task `flagdata`, which are listed in Extended Data Table 2.

Considering there are over 70 EBs with different tuning frequencies and configurations, caution is required to handle the visibility plane. The steep spectral slope of the dust continuum emission from the protocluster galaxies can lead to baseline-dependent flux densities, owing to the frequency variations of the different baselines, which can cause artificial signals in the Fourier-plane subtraction technique. We used all the data to produce ultra-deep continuum images for the direct tSZ decrement imaging ('Deep' and 'Deep (tapered)'), and used the subset of measurement sets with similar frequency ranges from Cycle 5 and Cycle 10 for source subtraction and tSZ measurements ('ALMA high-res', Extended Data Table 3).

The deep continuum map was generated with `tclean` using line-free channels, '`natural`' weighting, '`hogbom`' deconvolver, '`mosaic`' gridder in '`mfs`' mode. We applied a $2''$ uv taper to enhance sensitivity to extended emission. A two-step strategy was used for the `CLEAN`ing process. First, we `CLEAN`ed without a mask down to 4σ, ensuring real emission is deconvolved while avoiding noise spikes. Next, we masked the high-significance 4σ pixels and dilated them to the adjacent 2σ pixels. With this robust mask, we `CLEAN`ed the data to $\pm 1\sigma$, which suppresses dirty-beam sidelobes

and prevents over-`CLEAN`ing of noise spikes. The rms level of the `CLEAN`ed image is 1.8μJy/beam with a $2.4'' \times 2.1''$ synthesized beam before tapering, and 2.1μJy/beam with a $3.7'' \times 3.3''$ beam after tapering. In the 'Deep (tapered)' image (Extended Data Fig. 2), a negative halo around the protocluster galaxies reaches -4.5σ, which is present in the `CLEAN`ed and the residual images. The positive signal peaks at 116σ, which is comparable to the typical dynamic range achieved in ALMA Band-3 ($\sim 100\sigma$), supporting that features as faint as -4.5σ are reliable instead of an imaging artifact.

The tSZ signal is expected to contaminate the galaxies' continuum emission, which dominates the short spatial-frequency range. To produce a high-resolution continuum image for further source subtraction ('ALMA high-res'), we discarded the data with different frequency coverages (see Extended Data Table 3) and excluded all baselines with uv-distances less than 10kλ to suppress the extended tSZ contamination while still maintaining a good sensitivity. Under such a uv-distance selection, all signals with spatial scales above $20''$ are greatly reduced. We selected the line-free channels and used the identical two-step `CLEAN`ing strategy to produce the continuum map. With this uv range-selection strategy, the continuum flux density of each source is increased by $\sim 5\%$, while the rms sensitivity only drops by $\sim 1\%$. The synthesized beam size of the continuum image is $2.2'' \times 1.9''$ and the rms sensitivity is 2.1μJy/beam.

For the direct comparison of dust continuum under different scales, we also produced two independent low-resolution images from the short baselines ($< 10k\lambda$) of ALMA ('ALMA low-res') and from the ACA observations in a similar manner. The sensitivities of 'ALMA low-res' and ACA continuum images are $11\,\mu$Jy/beam and $24\,\mu$Jy/beam. Their corresponding resolutions are $14.4'' \times 13.4''$ and $18.0'' \times 12.1''$, respectively.

The details of each image, including the on-source exposure time, is summarized in Extended Data Table 3. The Maximum Recoverable Scale (MRS) of each map was estimated from the corresponding spatial scale of the fifth percentile value of the ALMA baseline lengths [74, 75]. The quoted value could overestimate the MRS when poorly-sample and less-weighted ACA data are included, which should be treated as the upper limit.

1.3 Photometry measurements of continuum-emitting galaxies

We used the `photutils` package for the photometry measurements of continuum-emitting galaxies from the 'ALMA high-res' map. The segmentation map was made using the `detect_sources` function with a 3σ threshold over 10 pixels. `deblend_sources` (npixels=5, nlevels=32, contrast=0.001) was applied to the segmentation map, which successfully deblended source 'D' and 'E' (C4 and C8). However, due to the sparse resolution, a few sources remain blended, which were treated as single sources during the measurements.

Subsequently, we made use of the `SourceFinder` function for the source extraction. To avoid noise contamination, we only extracted sources with a peak pixel value $> 4\sigma$. We recorded thee flux densities measured from their peak pixels and integrated values within standard kron apertures (`k=1.4, Rmin=2.5`), with the nearby sources all masked to prevent potential contamination. The aperture photometry uncertainty

was estimated by measuring the flux distribution in 10,000 randomly placed apertures of identical shape on the noise map. While the peak pixel can provide a more accurate measurement for unresolved sources, it cannot capture all emission when the source is extended. Therefore, we compared the flux densities obtained from these two methods and adopted the larger one as the 'best' flux density (Extended Data Table 4). However, due to the insufficient rms sensitivity and the potential contamination from the tSZ decrement, a few confirmed protocluster members were only marginally detected ($< 4\sigma$). For a conservative assessment of the tSZ signature, we did not include their contribution in the photometry measurement, which could cause a $\lesssim 30\mu$Jy underestimation of the total dust continuum within the core.

We also performed the continuum measurements using two independent datasets, the 'ALMA low-res' and 'ACA' maps, using identical methods. The continuum flux densities in both images are lower than the integrated values from individual galaxies measured from the high-resolution image (see Extended Data Table 4). The fainter emission is contrary to the general expectation from tapering, which usually shows higher fluxes for bright sources at the phase center [76, 77]. If the deviations are purely caused by the tSZ contamination, the signal of the tSZ decrement should be at least $131\pm32\,\mu$Jy. This 4.2σ deficit confirms the reliability of the 2.3σ difference seen in shallower data in previous work, which was speculated to be due to the tSZ contamination by Zhou et al. [14]. Because the tSZ decrement could be more extended than the size defined by continuum emission and the contribution of the faint sources was ignored, the intrinsic strength of the tSZ could be underestimated in this way.

1.4 Validation of the decrement with ALMA simulations

To test the reliability of the potential tSZ signatures, we conducted interferometric simulations using the CASA function simalma. We used the Band-7 catalog [12] as a prior and scaled the flux densities by $S_{3\mathrm{mm,total}}/S_{850\mu\mathrm{m,total}}$ to obtain the 3 mm flux density of each emissive source. As sensitivity can be underestimated by simalma, we tweaked the scaling factor of the telescope time in each configuration until the rms agreed with the actual value (Δrms/rms $< 5\%$). For a more realistic simulation, we also injected continuum sources on the jackknifed measurement sets, which were produced by inverting half of the visibilities to cancel the astrophysical signals.

Extended Data Fig. 3 shows the comparison between the simulations and the actual continuum image on the same scale. While the previous section reinforces the evidence of a tSZ decrement already seen as a negative halo in the real image, we also considered the possibility that the evidence of tSZ effect was caused by an interferometric artifact from combining different ALMA configurations. Although the issue of the negative sidelobes is greatly suppressed in such deep observations, imperfect CLEANing can be still expected, which may cause a similar negative halo. However, the coherent negative halo does not exist in the simulated image, where the minimum pixel value in the core region is only $4.5\,\mu$Jy, 1.7σ less than the decrement peak ($7.6\,\mu$Jy) in the actual continuum image. Furthermore, we used the same uv-range ($uv < 10k\lambda$) to produce the low-resolution mock image and performed the photometry measurements in an identical way. The continuum flux density from the low-resolution simulated map is consistent with the integrated value from the high-resolution image, which is contrary

11

to the 20% drop seen in the real data. Therefore, a potential artifact is unlikely to result in the current evidence of the tSZ decrement.

1.5 Continuum subtraction and tSZ measurement

To explore the morphology and actual strength of the negative signal free from contamination from dusty galaxies, we further subtracted the known continuum sources in the uv-plane. We used the CASA class `componentlist` to construct catalogs of continuum sources as point-like for the ACA and ALMA visibilities, while considering the primary beam attenuation. Next, we Fourier transformed the source list from the image plane to the uv-plane with the `ft` function and recorded the expected visibilities in the model column of each measurement set, which was then subtracted using the `uvsub` command from the calibrated visibilities.

With the continuum-subtracted data, we deconvolved the image created by the visibilities with uv distances $< 10k\lambda$ and generated an initial CLEANed image with the 'hogbom' deconvolver down to 4σ without the CLEAN mask. We masked pixels with an absolute value $> 4\sigma$ and expanded to the adjacent $> 2\sigma$ pixels. Then, we used the multi-scale deconvolver with scales of [0, 2, 4, 8] pixels and further CLEANed the data down to 1σ, resulting in an rms sensitivity of 8.8μJy/beam with a synthesized beam of $13.6'' \times 14.7''$. As shown in Extended Data Fig. 4, a strong decrement occurs at the center of the protocluster core [12], with the peak $\Delta(\text{R.A.}, \text{Dec.}) = (-7.2'', 2.1'')$ offset from the radio-loud AGN C.

The curve-of-growth analysis (Extended Data Fig. 6) indicates that the full width at half maximum (FWHM) of the decrement is $\text{FWHM}_{\text{SZ}} \approx 14''$ (100 kpc) with the signal extending out to $R_{\text{SZ}} \approx 20''$ (140 kpc) after correcting for beam broadening. This corresponds to an angular scale of $2R_{\text{SZ}} \sim 40'' \approx 5\,k\lambda$. The tSZ decrement is $-100 \pm 12\,\mu$Jy within R_{500} (80 kpc, [13]) and the total signal is $-157 \pm 16\,\mu$Jy. After correcting for projection effects [32], we calculated the Compton-Y parameter through the formula [7, 15, 30]

$$\Delta I_\nu = \frac{x^4 e^x}{(e^x - 1)^2} \left(x \frac{e^x + 1}{e^x - 1} - 4 \right) I_0 y = g(x) I_0 y, \tag{1}$$

where the CMB intensity $I_0 = 270.33\,$MJy/sr, ΔI_ν is the distortion signal in the CMB map (i.e., decrement intensity in the continuum map), and the dimensionless frequency $x = h\nu/kT_{\text{CMB}} = \nu/56.81\,$GHz ≈ 1.65. The Compton-y map is shown in Extended Data Fig. We obtained mean Compton-y parameters of $(10.2 \pm 1.3) \times 10^{-6}$ and $(5.6 \pm 0.8) \times 10^{-6}$ for within R_{500} and within R_{SZ}, respectively. The integrated tSZ signal (Compton-Y) can be calculated as [7]

$$Y_{\text{SZ}} = \int y\, d\Omega = \frac{1}{g(x)} \frac{1}{I_0} \int \Delta I_\nu d\Omega = \frac{S_\nu}{g(x) I_0}, \tag{2}$$

where Ω is the solid angle of the selected region, and S_ν is the flux density in the same region. This leads to Compton-Y parameters of $Y_{500} = (1.3 \pm 0.2) \times 10^{-6}\,$arcmin^2 and $Y_{\text{total}} = (2.0 \pm 0.2) \times 10^{-6}\,$arcmin^2.

However, considering the large radius of the tSZ decrement, analysis in the uv-plane is needed to evaluate if the signal is limited by insufficient short baselines. We used the `uvplot` package to export all associated data to a single uv table. The corresponding visibilities were then shifted to the position of the decrement peak. Extended Data Fig. 5 shows the visibilities as a function of uv distance, which were averaged over every $3k\lambda$. The uncertainties were estimated through the corresponding weight of each visibility. The positive signal of $\sim 30\,\mu$Jy at $10k\lambda$ is likely from the conservative continuum subtraction strategy, which is consistent with the estimation of the total under-subtraction signal $\sim 30\,\mu$Jy. Extended Data Fig. 5 shows that the amplitude of the negative signal profile peaks at the shortest uv distance of $\sim 3k\lambda$ with a large uncertainty, indicating that the current data have less capability in recovering the signal at this scale. This suggests that the signal can approach or even go beyond the MRS and its angular scale should be $\lesssim 6k\lambda$ ($\gtrsim 35''$ or $240\,$kpc), which is consistent with the analysis conducted in the image plane. Because of the large uncertainty in the shortest uv distance and the primary beam attenuation for such a large scale signal, the intrinsic tSZ signal cannot be directly measured in the uv-plane and a model-dependent value is out of the scope of this letter, which is planned for a future paper.

1.6 Comparison with other tSZ systems

To place our tSZ detection in a broader context, we compiled a sample of systems with tSZ detections, including low-redshift galaxy clusters with weak-lensing mass estimates [37–39] and high-redshift systems ($z \gtrsim 2$) with tSZ detections [8–10, 40, 72]. Since the reported tSZ decrements are derived from different methods and expressed in different units, we adopted a universal pressure profile ('arnaud10') to convert all results to the spherical Y_{500} integrated within R_{500} in units of Mpc^2 for consistency [32]. For high-redshift systems, we also used the 'diemer19' halo concentration profile to convert the virial masses estimated from velocity dispersions to M_{500} values [78, 79], as most targets lack weak-lensing mass calibration.

The ICM is known to evolve self-similarly with redshift. To compare our detected tSZ signal to the expected $M-Y$ relation, we removed the redshift dependence by factoring out the $E(z)^{2/3}$ scaling for each system. As shown in Extended Data Fig. 8, most low-redshift systems follow the relation $Y_{500} \propto M_{500}^{1.79}$ [34]. However, with the exception of Cl1449, high-redshift systems show a larger scatter and lie below the values predicted by the universal relation, in contrast to the tighter relation at $z \sim 2$ predicted by current simulations [44]. This discrepancy can be explained by the presence of cooler, unvirialized ICM in the early stages of cluster formation [4]. Nevertheless, the tSZ decrement we observed is a factor of five larger than the predicted value, suggesting significantly higher gas pressure in SPT2349$-$56 at a much earlier epoch.

1.7 Thermal energy budget of the nascent ICM

To examine if the decrement can be caused by gravity, we calculated the thermal energy required by the measured tSZ signal and possible gravitational energy of the virialized gas.

13

We estimated the total thermal energy using the equation [31]

$$E_{\text{therm}} = 2.9 \frac{m_e c^2}{\sigma_T} l_{\text{ang}}^2 \int y \, d\Omega = 2.9 \times 10^{60} \text{erg} \left(\frac{l_{\text{ang}}}{\text{Gpc}} \right)^2 \frac{Y_{\text{SZ}}}{10^{-6} \text{arcmin}^2}, \quad (3)$$

where the angular diameter distance to the source $l_{\text{ang}} = 1.42 \, \text{Gpc}$. We obtained a total thermal energy of $E_{\text{therm,total}} = (11.8 \pm 1.2) \times 10^{60}$ erg and $E_{\text{therm,500}} = (7.5 \pm 0.9) \times 10^{60}$ erg within the R_{500} radius.

To assess if this thermal energy can be matched to the energy of a thermal-equilibrium ICM, we need to explore its constraint on halo mass (M_{200}), ICM temperature (T_{ICM}), and ICM fraction ($f_{\text{ICM}} = \text{M}_{\text{ICM}}/\text{M}_{200}$). The halo mass M_{200} can be obtained by

$$M_{200} = \frac{2E_{\text{therm}} \mu m_p}{3 f_{\text{ICM}} k_B} \frac{1}{T_{\text{ICM}}}, \quad (4)$$

where the molecular weight $\mu \approx 0.6$, proton mass $m_p \approx 1.67 \times 10^{-24}$ g, and f_{ICM} is the mass ratio between the dark matter halo and the hot ICM. Here we assumed that the thermal energy within R_{200} radius is $E_{\text{therm,200}} \approx E_{\text{therm,total}}$. This is a good approximation because $R_{200} = 18.5'' \times (M_{200}/10^{13} M_\odot)^{1/3}$, which is comparable to the tSZ radius $R_{\text{SZ}} \approx 20''$.

Next, we calculated the gas temperature for a virialized ICM. For simplicity, we used the mean virial temperature $\langle T_{200} \rangle$ within R_{200} given by Voit [6],

$$k_{\text{B}} T_{\text{vir}} \approx k_{\text{B}} \langle T_{200} \rangle = \frac{G M_{200} \mu m_p}{2 R_{200}}, \quad (5)$$

where the gravitational constant $G \approx 6.67 \times 10^{-11} \, \text{m}^3 \, \text{kg}^{-1} \, \text{s}^{-2}$. The mass M_{200} and radius R_{200} of the halo have the following relation

$$M_{200} = \frac{4}{3} \pi R_{200}^3 \rho_{200}. \quad (6)$$

Combining Eq. 5 and Eq. 6, we can obtain the relation between M_{200} and T_{vir} for a virialized halo

$$M_{200} = \left(\frac{6}{\pi \rho_{200}} \right)^{1/2} \left(\frac{k_B}{G \mu m_p} \right)^{3/2} T_{\text{vir}}^{3/2}. \quad (7)$$

If the system is virialized with a halo mass $M_{200} = (9 \pm 5) \times 10^{12} M_\odot$ [12], we can derive a total thermal energy of $(f_{\text{ICM}}/0.02) \times (8.5 \pm 3.2) \times 10^{59}$ erg, which is negligible compared to the ICM thermal energy. Even assuming an extremely abundant ICM $f_{\text{ICM}} = 6\%$ [13], the derived thermal energy is only $(2.6 \pm 1.0) \times 10^{60}$ erg, $\sim 20\%$ of the value inferred by the observed decrement. Under this condition, the estimated thermal energy corresponds to a Compton-Y parameter of $Y = (4.4 \pm 0.4) \times 10^{-7} \text{arcmin}^2$ or a distortion signal of $34 \pm 4 \, \mu\text{Jy}$. For a $9 \times 10^{12} M_\odot$ halo, it is unlikely that gravity serves as the dominant energy source for the observed tSZ signal.

We then explored the possible halo masses and ICM temperatures allowed by the tSZ decrement. The mass of the hot ICM is limited by the available baryonic budget

in the halo. We have a lower limit of the halo mass of

$$M_{200} \geq \frac{1}{f_b - f_{\mathrm{ICM}}}(M_{\mathrm{mol}} + M_*), \tag{8}$$

where f_b is the baryonic fraction of the protocluster. In the following calculation, we adopted the universal baryonic fraction $f_b = 0.155$. For a conservative estimate, we used $r_{41} = 0.60$ and $\alpha_{\mathrm{CO}} = 1\,\mathrm{M_\odot}/(\mathrm{K\,km\,s^{-1}\,pc^2})$ to calculate the molecular gas mass M_{mol} from the CO(4–3) luminosity of SPT2349−56 [14]. As a result, M_{mol} and M_* of SPT2349−56 are $4.9 \times 10^{11}\,\mathrm{M_\odot}$ and $6.3 \times 10^{11}\,\mathrm{M_\odot}$, respectively (Pillai et al. in prep).

The parameter space constrained by the measured tSZ decrement and the available baryons is shown in Extended Data Fig. 9. Within the possible M_{ICM} range and without assuming an extreme f_{ICM}, either a more massive virialized halo or a super-virialized ICM gas is necessary to match the observed tSZ decrement.

In the case that the thermal energy is under thermal equilibrium in an extremely massive halo, we can obtain

$$M_{200} \approx (4.4 \pm 0.5) \times 10^{13} M_\odot \times \left(\frac{0.02}{f_{\mathrm{ICM}}}\right)^{3/5}. \tag{9}$$

Assuming a regular ICM fraction of $f_{\mathrm{ICM}} \lesssim 0.02$ at $z > 4$, the expected halo mass will be more than five times the halo mass derived from velocity dispersion [12], which is unlikely given the compactness of the system.

1.8 Redshift evolution of ICM in TNG-Cluster simulations

We compared our measured tSZ signal with predictions from the TNG-Cluster zoom-in simulations of massive galaxy clusters [80, 81]. In brief, TNG-Cluster comprises a suite of 352 high-resolution re-simulations of massive clusters selected from a parent dark matter-only simulation with a box size of $\sim 1\,\mathrm{Gpc}$. The sample includes all clusters at $z = 0$ with $M_{200} > 10^{15}\,M_\odot$, along with a representative subset of lower-mass systems spanning $M_{200} \sim 10^{14.3}$–$10^{15.0}\,M_\odot$. As with the IllustrisTNG framework, TNG-Cluster employs the `AREPO` moving-mesh magnetohydrodynamics code [82, 83], together with the TNG galaxy formation model [84, 85], which self-consistently follows the evolution of gas, stars, supermassive black holes, chemical enrichment, and feedback from both stellar and AGN sources.

For this analysis, we used the TNG-Cluster predictions to compare the thermal component of the gas to that inferred for the SPT2349−56 protocluster core. Specifically, we computed the Compton-y parameter following the prescriptions of Bigwood et al. [28], Nelson et al. [81], Roncarelli et al. [86], Kay et al. [87], McCarthy et al. [88], which are virtually equivalent. For each gas cell, the y parameter (Υ_i) was computed as

$$\Upsilon_i = \frac{k_B \sigma_T}{m_e c^2} N_{e,i} T_i, \tag{10}$$

where k_B is Boltzmann's constant, σ_T the Thomson scattering cross-section, m_e the electron mass, and c the speed of light. Here, $N_{e,i}$ and T_i represent the number of

15

electrons and the temperature of the i-th gas cell, respectively. The number of electrons was computed as $N_{e,i} = n_{e,i} m_i / \rho_i$, where $n_{e,i}$ is the electron number density, m_i is the gas cell mass, and ρ_i is the gas density.

In practice, we derived Υ_i for each gas cell using `InternalEnergy` (U), `ElectronAbundance` (X_e), and `Masses` (m_i) from the TNG-Cluster outputs. The temperature of each gas cell was then calculated as

$$T_i = \frac{U(1-\gamma)\mu}{k_B},\tag{11}$$

where $\gamma = 5/3$ is the adiabatic index and μ is the mean molecular weight, given by:

$$\mu = \frac{4}{1 + 3X_H + 4X_H X_e} m_p,\tag{12}$$

with X_H the hydrogen mass fraction (assumed to be $X_H = 0.76$) and m_p the proton mass. The number of electrons was computed as:

$$N_{e,i} = \frac{n_{e,i} m_i}{\rho_i} = \frac{X_e X_H m_i}{m_p}.\tag{13}$$

To compute $N_{e,i}$ and T_i for each gas cell, we adopted a fixed hydrogen mass fraction of $X_H = 0.76$, following common assumptions in the literature [81, 87]. Although one might expect a higher hydrogen fraction at earlier epochs, we verified that the median hydrogen abundance in gas cells associated with the TNG-Cluster halo at $z \sim 5$ remains close to $X_H \sim 0.76$.

The integrated tSZ signal for a given halo, expressed as $Y_{500} D_A^2$, was calculated by summing the Υ_i contributions (from Equation 10) of all gas cells within a spherical aperture of radius R_{500}. We then tracked the redshift evolution of this tSZ proxy by evaluating Y_{500} for the main progenitors of all 352 clusters identified at $z = 0$ within the TNG-Cluster suite. We traced Y_{500} of each cluster for every four snapshots and calculated the 16th, 50th, and 84th percentile values in each redshift bin. The evolution of the fraction of hot gas $> 10^7\,\mathrm{K}$ within the R_{500} radius ($f_{\mathrm{hot}} = M_{\mathrm{hot},500}/M_{500}$) was also recorded to investigate the simulation expectation for the hot gas at earlier epochs. The Y_{500} values were scaled by $M_{500}^{1.79}$ to removed the mass dependency [34].

We show the 16th-50th-84th percentile values of the mass-scaled Y_{500} and f_{hot} at $0 \le z \le 5$ for each redshift bin in Fig. 1 and Extended Data Fig. 10, respectively. As indicated by Fig. 1, the tSZ decrement observed in SPT2349$-$56 is also more than five times the value predicted by TNG-Cluster. Without assuming a very massive halo (Extended Data Fig. 9), the lower hot-gas fraction or a cooler ICM in TNG-Cluster is likely the reason of this discrepancy.

1.9 Possible energy injection from non-gravitational processes

In addition to energy from gravitational processes, AGN and star-formation activities are likely to provide the additional energy injection needed to explain the large thermal reservoir inferred by the observed tSZ decrement. Given that kinetic energy is

the dominant source besides gravitational energy for large-scale heating [58], we only consider its contribution to the thermal energy of the nascent ICM in SPT2349−56 for simplicity.

1.9.1 Kinetic-mode AGN feedback

Previous studies indicate that AGN activity is significantly enhanced in SPT2349−56 [13, 89]. At least three protocluster members show strong radio excess, with a total rest-frame 1.4 GHz power of $L_{1.4\,\mathrm{GHz}} = (2.2 \pm 0.3) \times 10^{26}$ W/Hz (Chapman et al. in prep), of which one is also luminous in X-rays [89]. From their modest radio luminosities, Chapman et al. [13] speculates that the detected radio AGN can be fueled by hot gas in radio-mode instead of radiative-efficient accretion through recent mergers, which can provide strong kinetic feedback with substantial energy injection on the nascent ICM in the protocluster. We used the correlation between the cavity power (P_{cav}) and radio luminosity at 1.4 GHz ($L_{1.4\,\mathrm{GHz}}$) to estimate the kinetic power from radio luminosity alone, which can be described using [90]

$$P_{\mathrm{cav}} = 7 \times 10^{43}\,\mathrm{erg/s} \times f_{\mathrm{cav}} \left(\frac{L_{1.4\,\mathrm{GHz}}}{10^{25}\,\mathrm{W\,Hz^{-1}}} \right)^{0.68}, \tag{14}$$

where the enthalpy factor $f_{\mathrm{cav}} = 4$ for relativistic plasma. Shocks induced by the radio jet can cause additional heating, which could imply a higher $f_{\mathrm{cav}} > 4$ [55, 91]. This scaling relation yields a kinetic power of $\dot{E}_{\mathrm{kin,radio}} = (2.3 \pm 0.3) \times 10^{45}\,\mathrm{erg/s} \times (f_{\mathrm{cav}}/4)$.

1.9.2 Radiative-mode AGN feedback

On the other hand, the protocluster galaxy 'A' (or 'C1') is luminous in X-ray with an AGN luminosity of $L_{\mathrm{AGN}} = (1.9 \pm 0.7) \times 10^{47}\,\mathrm{erg/s}$ [89], which can also power large-scale outflows through radiation pressure when the outflow exceeds the local escape velocity [54, 58]. We can use the tight correlation between AGN luminosity and outflow rate to estimate the kinetic power from the radiation pressure:

$$\dot{E}_{\mathrm{kin,rad}} = f_{\mathrm{rad}} \times L_{\mathrm{AGN}}, \tag{15}$$

where the coupling efficiency of radiative-mode feedback $f_{\mathrm{rad}} \approx 0.5\%$ [53, 92]. We note that energy can be injected to the forming ICM only when outflows overcome the potential well of the host galaxy. The corresponding escaping power is

$$\dot{E}_{\mathrm{esc,rad}} = f_{\mathrm{esc,rad}} \dot{E}_{\mathrm{kin,rad}} = \left[1 - \left(\frac{v_{\mathrm{esc}}}{v_{\mathrm{out}}} \right)^2 \right] \dot{E}_{\mathrm{kin,rad}}, \tag{16}$$

where $f_{\mathrm{esc,rad}}$ is the escape efficiency for the radiation-driven outflow, $v_{\mathrm{esc}} = \sqrt{2GM/R}$ is the escape velocity from the host galaxy, and v_{out} is the velocity of AGN outflow driven by the radiative feedback. With the assumed AGN-outflow velocity of $v_{\mathrm{out}} \approx 1000\,\mathrm{km/s}$, estimated dynamical mass $M_{\mathrm{dyn}} \approx 2.7 \times 10^{11}\,\mathrm{M_\odot}$, and galaxy radius $R \approx$

6 kpc [12, 93], the escape efficiency is $f_{\mathrm{esc,rad}} \approx 0.6$. The escaping kinetic power from 'A' is $\dot{E}_{\mathrm{sec,rad}} = (0.6 \pm 0.2) \times 10^{45}\,\mathrm{erg/s} \times (f_{\mathrm{esc,rad}}/0.6) \times (f_{\mathrm{rad}}/0.005)$.

1.9.3 Star formation

We next consider energy injection from star formation activity. The kinetic power from star formation-driven outflows is given by [13, 94]

$$\dot{E}_{\mathrm{esc,SF}} \approx \frac{1}{2}\dot{M}_{\mathrm{out,SF}} v_{\mathrm{out,SF}}^2 f_{\mathrm{esc,SF}}, \tag{17}$$

where $f_{\mathrm{esc,SF}}$ is the escape efficiency of an outflow and the mass outflow rate $\dot{M}_{\mathrm{out,SF}}$ is related to the SFR by the mass-loading factor $\eta = \dot{M}_{\mathrm{out,SF}}/\mathrm{SFR} \approx 1$. Given an SFR of $\sim (5000 \pm 600)\,\mathrm{M}_\odot/\mathrm{yr}$ in the protocluster core [11–13], the kinetic power from star formation is $\dot{E}_{\mathrm{esc,SF}} = (0.8 \pm 0.1) \times 10^{44}\,\mathrm{erg/s} \times (v_{\mathrm{out,SF}}/500\,\mathrm{km\,s^{-1}})^2 \times (f_{\mathrm{esc,SF}}/0.2)$, which is less than 5% of the kinetic power from AGN feedback. We therefore conclude that energy injection from star formation can be safely neglected.

1.9.4 Total energy injection and thermal coupling efficiency

Assuming $f_{\mathrm{cav}} = 4$, $f_{\mathrm{esc,rad}} = 0.6$, and $f_{\mathrm{rad}} = 0.005$, we can estimate the total energy input:

$$\begin{aligned}
\Delta E_{\mathrm{inject}} &\approx \dot{E}_{\mathrm{kin,radio}} t_{\mathrm{radio}} + \dot{E}_{\mathrm{esc,rad}} t_{\mathrm{rad}} \\
&= \left[(7.3 \pm 0.9) \times \left(\frac{t_{\mathrm{radio}}}{100\,\mathrm{Myr}} \right) + (1.8 \pm 0.7) \times \left(\frac{t_{\mathrm{rad}}}{100\,\mathrm{Myr}} \right) \right] \times 10^{60}\,\mathrm{erg}.
\end{aligned} \tag{18}$$

Adopting $t_{\mathrm{AGN}} = 100\,\mathrm{Myr}$ for AGN activities, we can obtain a total energy injection of $(9.1 \pm 1.1) \times 10^{60}\,\mathrm{erg}$ to be stored in the nascent ICM.

According to thermodynamics and the ideal gas law, the kinetic energy is known to have two effects. The injected energy can lead to a system expansion against the ambient pressure or an increase in the thermal energy of the ICM, which can be expressed as

$$\Delta E_{\mathrm{inject}} \propto \int P\mathrm{d}V + \int V\mathrm{d}p = \Delta E_{\mathrm{therm}} + W_{\mathrm{expan}} = \frac{\Delta E_{\mathrm{therm}}}{f_{\mathrm{therm}}}, \tag{19}$$

where $\Delta E_{\mathrm{therm}}$ is the thermal energy change due to the pressure increase, W_{expan} is the expansion work, and the thermal energy coupling efficiency f_{therm} is defined as the fraction of kinetic power increasing the thermal energy instead of the bulk work. Assuming that the halo is virialized with $f_{\mathrm{ICM}} = 0.02$, the thermal energy change is $\Delta E_{\mathrm{therm}} = E_{\mathrm{therm}} - E_{\mathrm{therm,vir}} = (10.9 \pm 1.2) \times 10^{60}\,\mathrm{erg}$.

These assumptions imply a thermal coupling efficiency of $f_{\mathrm{therm}} = 120 \pm 20\%$, indicating that our energy injection must be underestimated. To reproduce the observed tSZ decrement, at least one of the following parameters must exceed our fiducial values:

- The cavity enthalpy factor $f_{\mathrm{cav}} > 5$ instead of 4;

- The AGN active time $t_{\mathrm{AGN}} > 120\,\mathrm{Myr}$ instead of $100\,\mathrm{Myr}$;
- The radiative-mode coupling efficiency $f_{\mathrm{rad}} > 1\%$ instead of 0.5%;
- The fraction of hot ICM $f_{\mathrm{ICM}} > 6\%$ instead of 2%;
- The halo mass $M_{200} > 1.7 \times 10^{13}\,M_{\odot}$ instead of $0.9 \times 10^{13}\,M_{\odot}$.

We note that the kinetic-mode AGN feedback can supply substantially more energy, which naturally explains the inferred thermal energy. The radio AGN in SPT2349$-$56 exhibit steep spectral slopes ($\alpha < -1$, Chapman et al. in prep), indicating relatively old ages. Chapman et al. [13] point out that the steep spectral slope, along with the compact size of the radio AGN, implying a potential compact steep spectrum source, which could lead to an age exceeding $500\,\mathrm{Myr}$. Moreover, the enthalpy factor f_{cav} can exceed the canonical value when the ambient gas pressure is high. Indeed, the ambient pressure can be sufficient enough to confine jets and enhance shock heating in some radio galaxies [56, 95–98]. At $z > 4$, the ICM pressure are higher due to the elevated cosmic critical density, which naturally provides a strong confining pressure for the surrounding medium [99]. The enhanced pressure can also limit system expansion, which boosts f_{therm} by suppressing the PdV term, resulting a large thermal energy reservoir in the nascent ICM at $z > 4$.
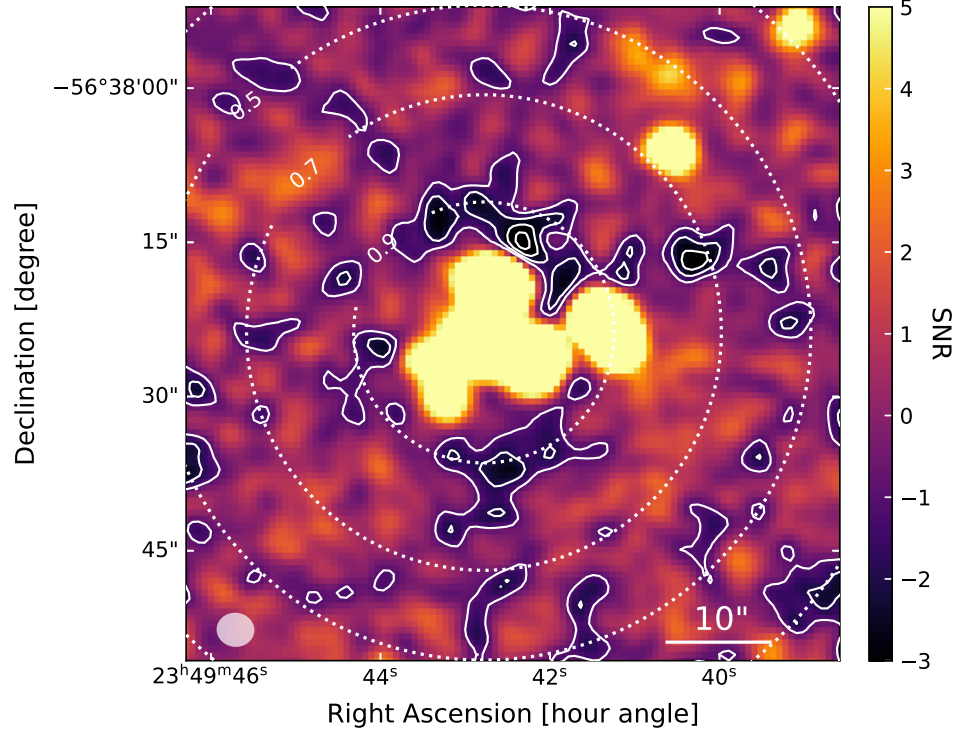
Extended Data Fig. 1 Tapered ALMA+ACA 3 mm continuum map. The positive signals come from dust emission of DSFGs. We use the contours from -1σ to -4σ with steps of -1σ to highlight the negative signals. The synthesized beam is shown in the bottom-left corner and the primary beam responses of 0.3, 0.5, 0.7, and 0.9 are indicated as dotted lines. A consistent negative ring is seen around the protocluster core, with a peak value at -4.5σ, suggesting the existence of extended tSZ signal.
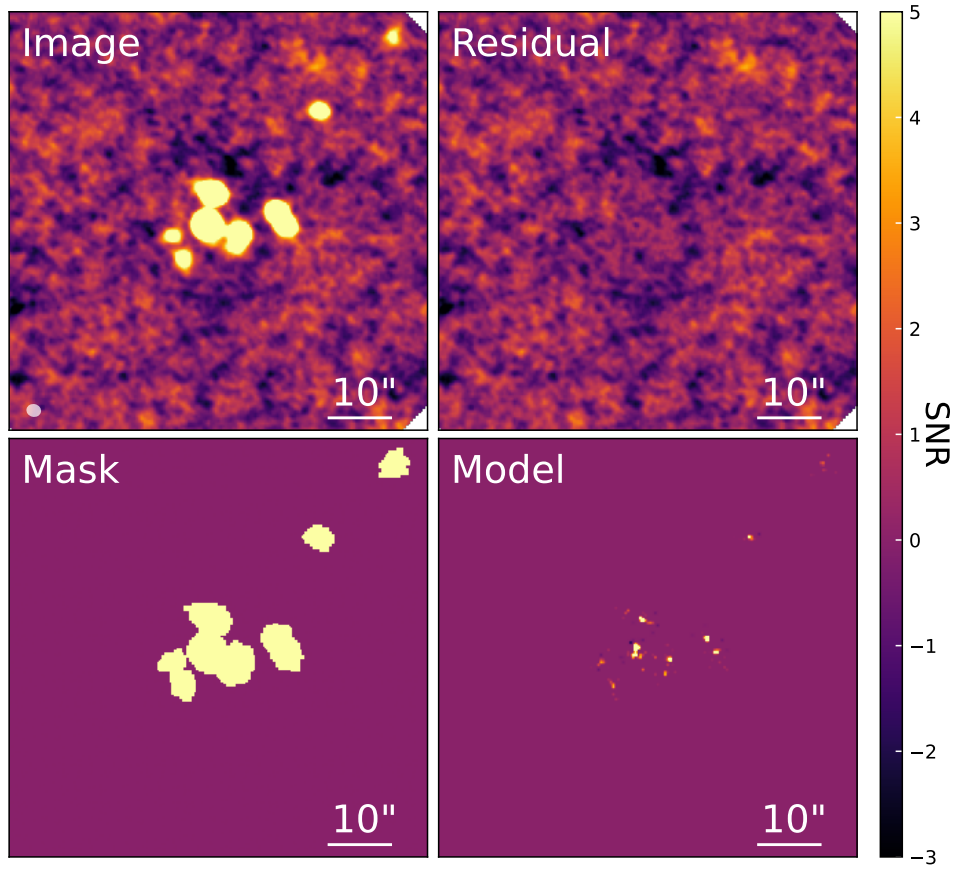
Extended Data Fig. 2 CLEANing process for the 'deep' imaging. To avoid negative sidelobes from the dirty beam, we perform a deep CLEANing down to the 1σ level, with the CLEANing mask and model indicated in the bottom panels. The synthesized beam is shown in the bottom-left corner of the upper-left panel. Despite the fact that no obvious emission is left after CLEANing, the negative halo persists in the residual image (top right).
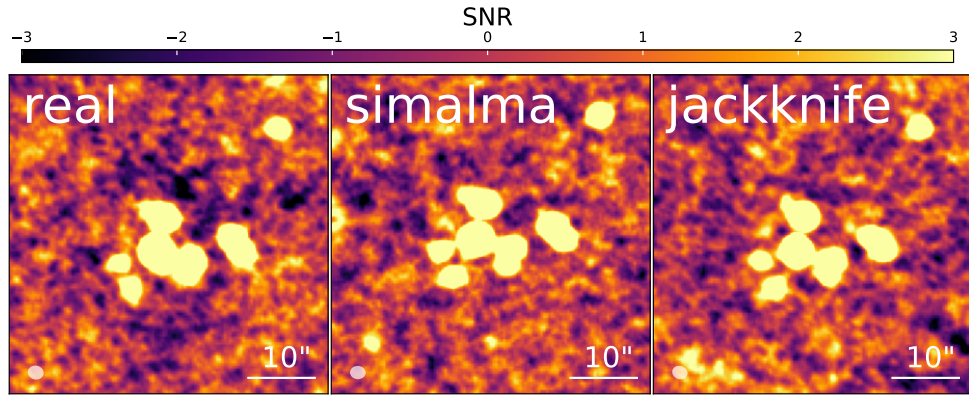
Extended Data Fig. 3 Comparison between the real and simulated images. We created simulated continuum images to further investigate if the negative halo can be caused by any unknown interferometric artifacts due to the complex distribution of the bright DSFGs. The corresponding synthesized beam is shown in the bottom-left corner for each panel. The minimum pixel value from the real map is 1.7σ more significant than both simulated maps, and the simulated maps do not display a coherent negative ring seen in the real image.
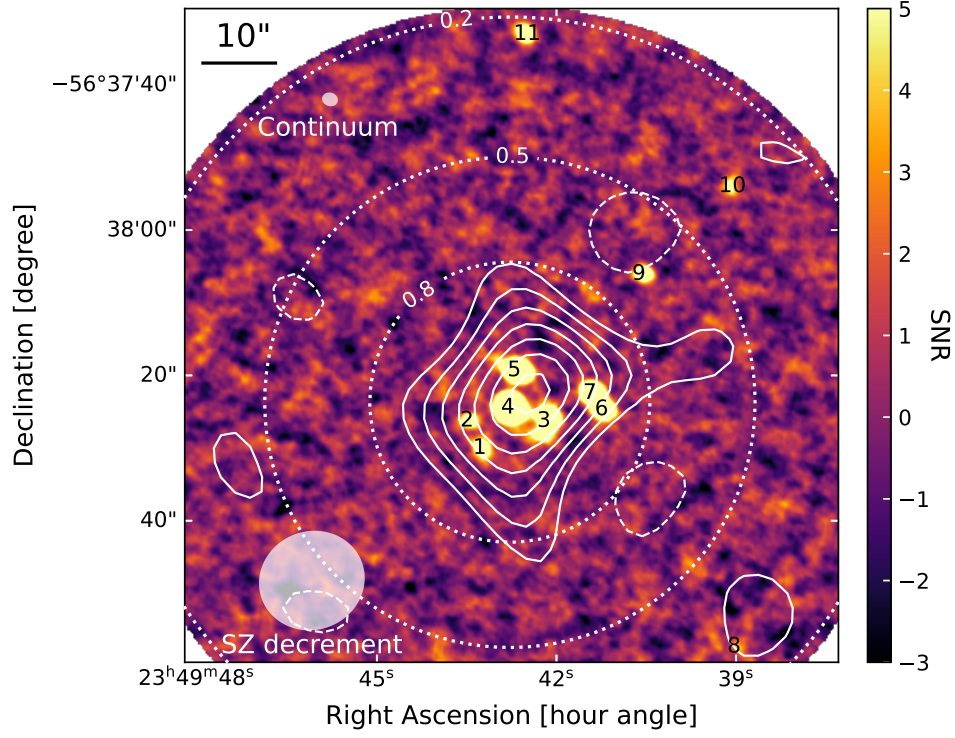
Extended Data Fig. 4 ALMA high-resolution continuum map with the tSZ contours.
The solid contours are from -2σ to -8σ with steps of -1σ. The dashed contours indicate regions with values above 2σ. The primary beam responses are indicated as dotted lines. The synthesized beams of the continuum image ('ALMA high-res') and the SZ decrement ('SZ') are indicated in the upper left and the bottom-left corners, respectively.
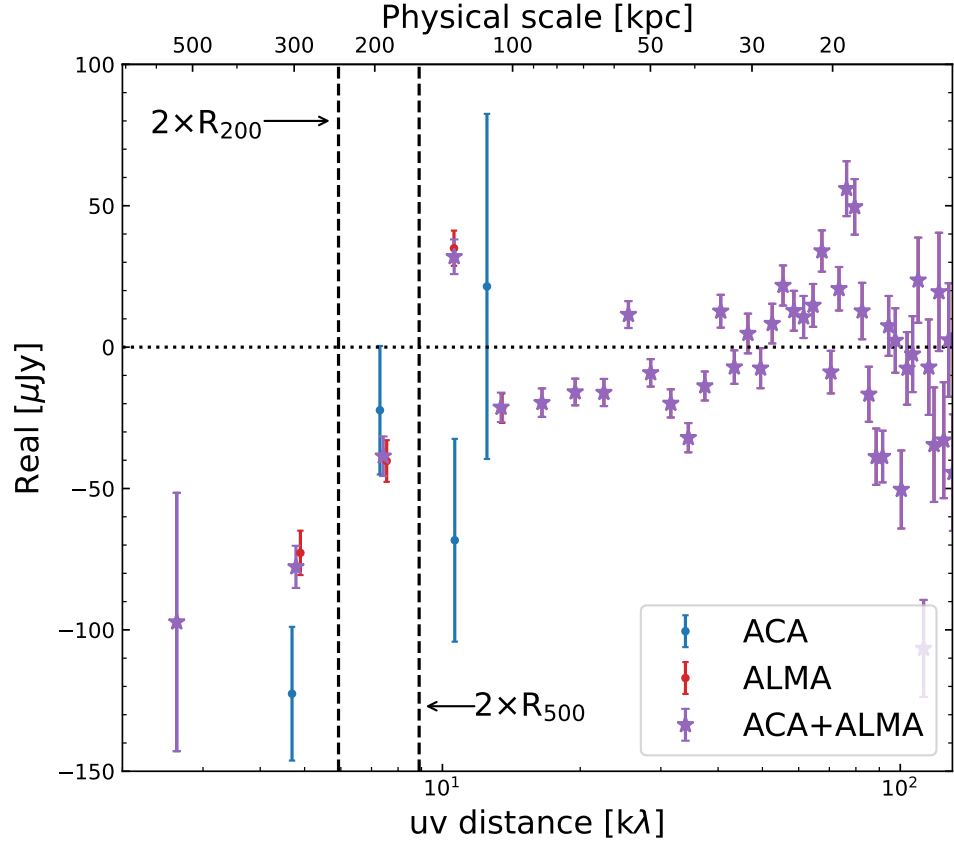
Extended Data Fig. 5 *uv* **profile of the continuum subtracted data.** The real part of the averaged amplitude measured from the continuum-subtracted measurement sets as a function of *uv*-distance with *uv* bins of $3k\lambda$. The negative signal becomes stronger at a shorter *uv* distance, suggesting that the tSZ decrement can be limited by the *uv*-coverage of the ACA and ALMA observations.
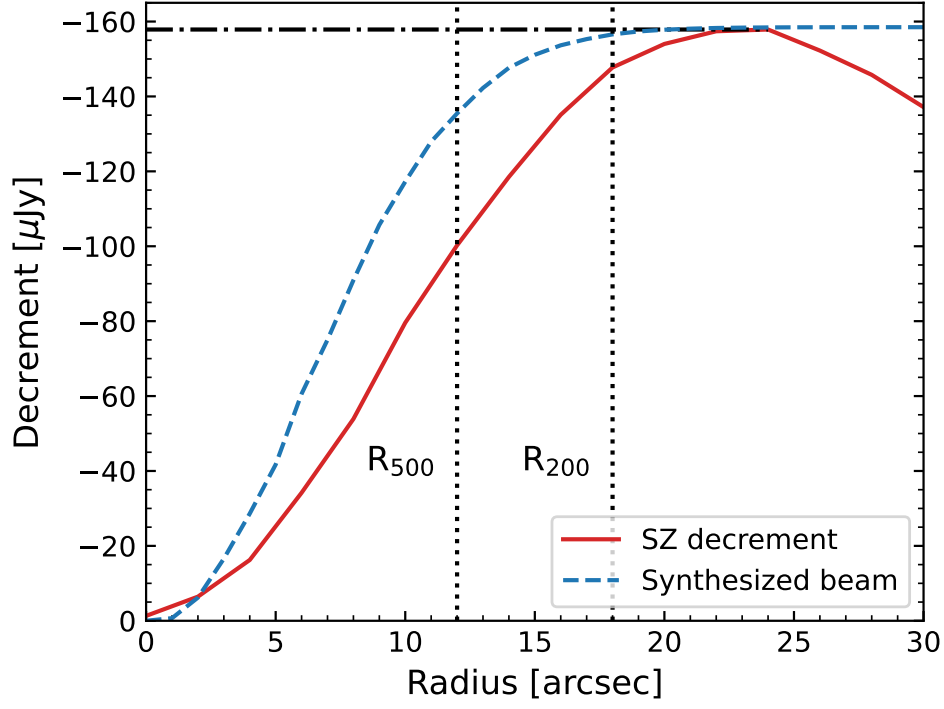
Extended Data Fig. 6 Curve-of-growth analysis for the tSZ decrement. The flux density of the tSZ decrement and the flux-scaled synthesized beam of the 'SZ' map are indicated as the red solid and the blue dashed line, respectively. The overdensity radii are also shown as black dotted lines. The decrement turnaround at radii $\gtrsim 25''$ may indicate potential dirty-beam sidelobes from imperfect CLEANing process.
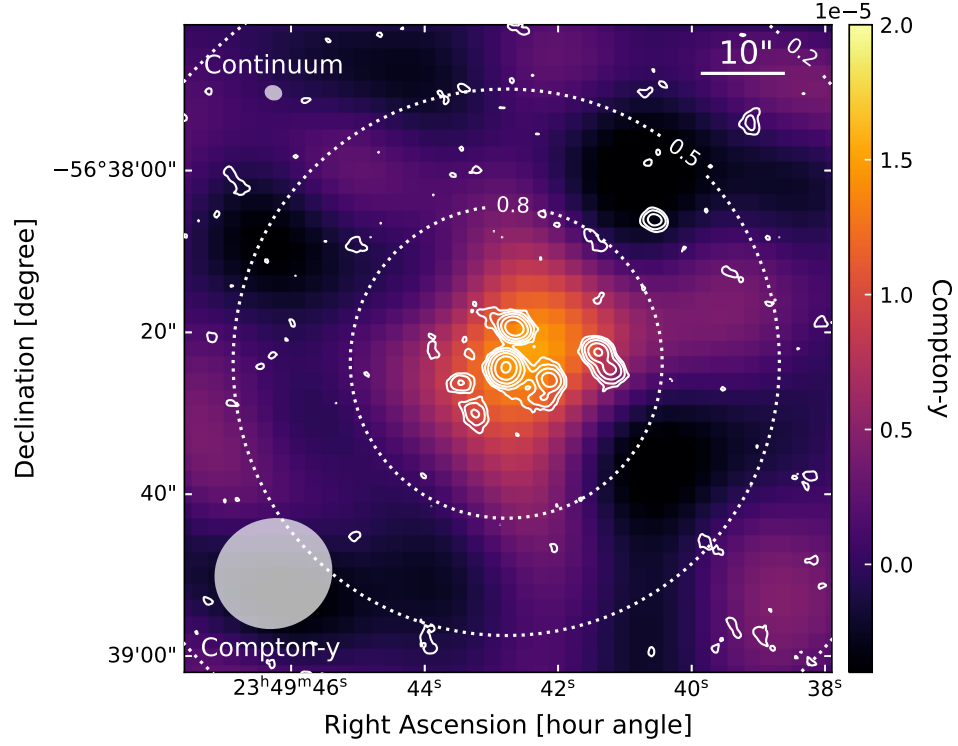
Extended Data Fig. 7 Compton-y map with dust continuum contours. The solid contours are 3 mm continuum emission drawn at $[2.5\sigma, 5\sigma, 10\sigma, 20\sigma, 40\sigma, 80\sigma]$ from the 'ALMA high-res' map. The primary beam responses are indicated at dotted lines. The synthesized beams of 3 mm continuum and Compton-y map are indicated in the upper-left and the bottom-left corners.
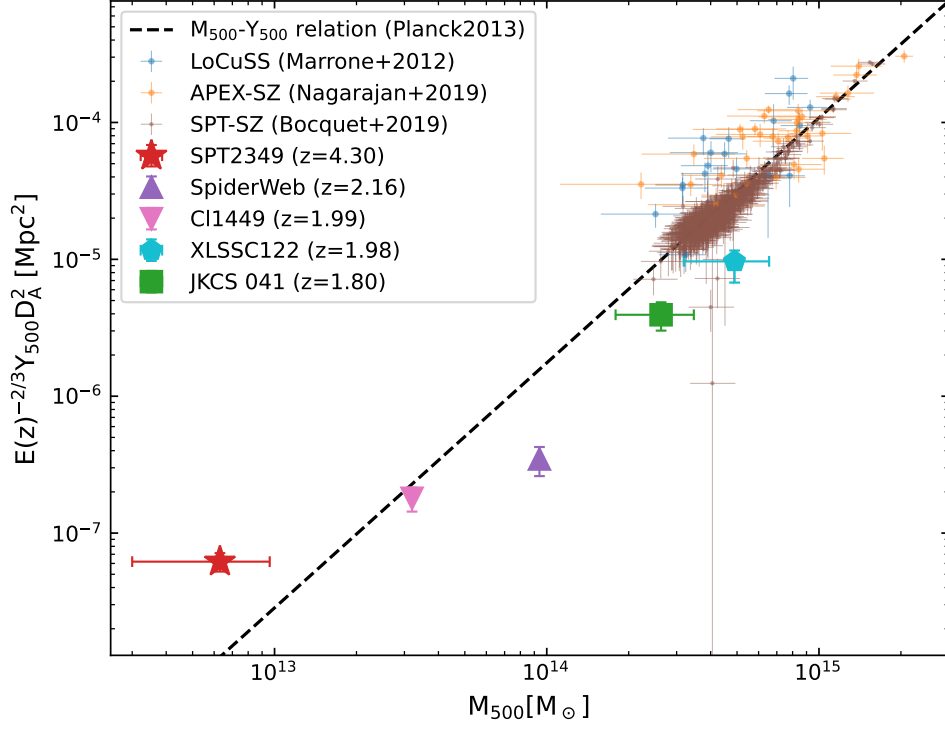
Extended Data Fig. 8 TSZ signal Y_{500} as a function of halo mass M_{500} within R_{500}.
The halo masses M_{500} and Compton-Y Y_{500} are same as in Fig. 1. The self-similar redshift evolution
have been taken into account by including a factor of $E(z)^{-2/3}$. The dashed line shows the universal
$M_{500} - Y_{500}$ relation reported by Planck Collaboration et al. [34].
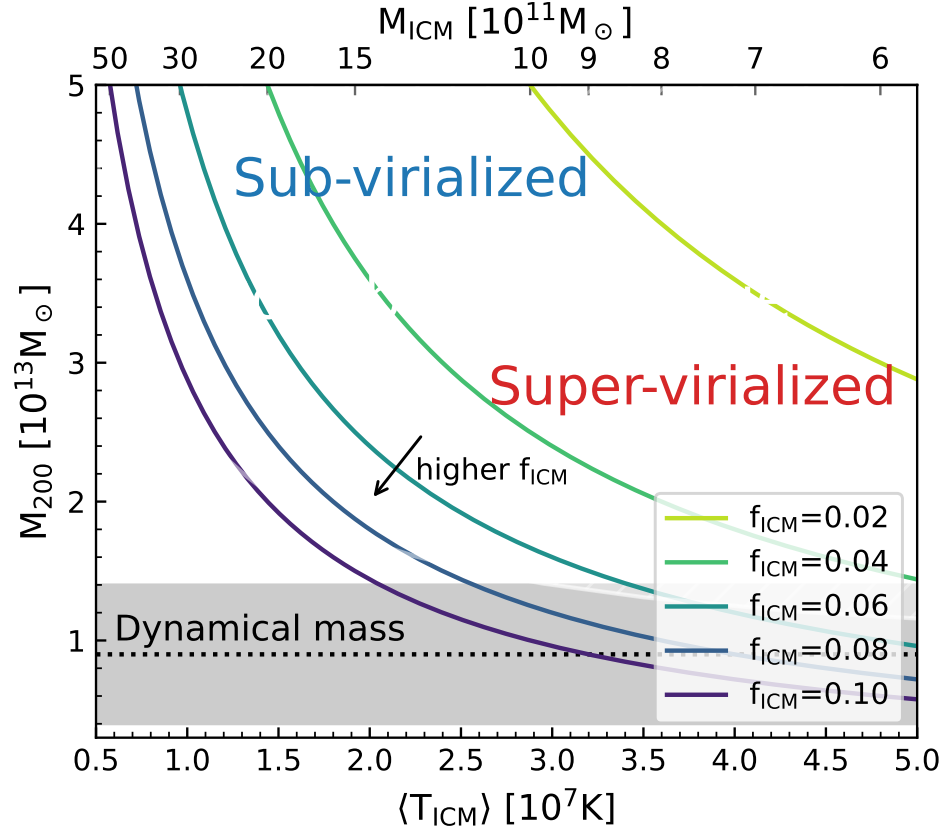
Extended Data Fig. 9 Halo mass as a function of ICM temperature. The corresponding ICM mass M_{ICM} is indicated in the top axis. The sub-virialized (blue) and super-virialized (red) regions are separated by the virialized temperature for different M_{200}. The dotted line indicates the dynamical mass of SPT2349−56 [12]. The lighter upper region is the possible M_{ICM} range allowed by the universal baryonic fraction $f_b = 0.155$. Without assuming an extreme ICM fraction f_{ICM}, either a more massive virialized halo or a super-virialized ICM gas is necessary to match the observed tSZ decrement.
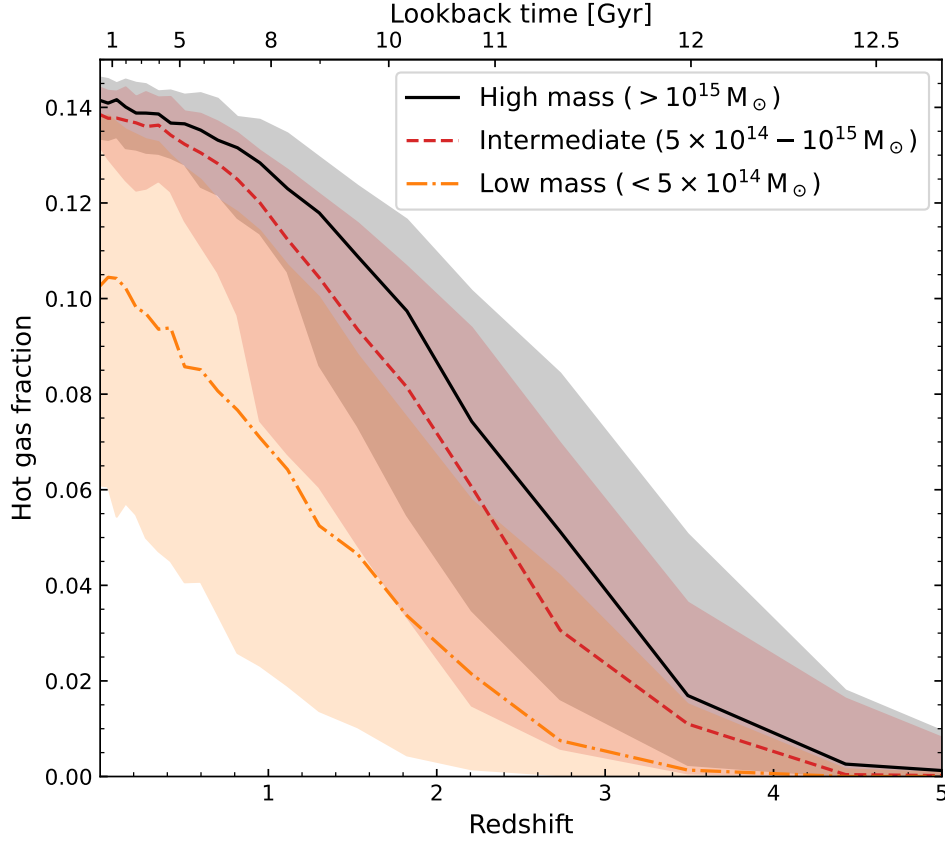
Extended Data Fig. 10 Cosmic evolution of the hot gas ($> 10^7$ K) fraction in galaxy clusters. The fraction of hot ICM ($\mathrm{M_{hot\,ICM,500}/M_{500}}$) within r_{500} as a function of redshift obtained from the TNG-Cluster simulation. Based on the total mass $\mathrm{M_{200}}$ at $z = 0$, the clusters are placed in three mass bins, high mass ($\mathrm{M_{200}} > 10^{15}\,\mathrm{M_\odot}$, black solid line), intermediate mass ($5 \times 10^{14}\,\mathrm{M_\odot} < \mathrm{M_{200}} < 10^{15}\,\mathrm{M_\odot}$, red dashed line), and low mass ($\mathrm{M_{200}} < 5 \times 10^{14}\,\mathrm{M_\odot}$, orange dash-dotted line). The corresponding shaded regions represent the values between the 16th and 84th percentiles in individual mass bins.

Extended Data Table 1 Summary of ALMA observations used in this study.

Program ID	Configuration	L_{base} [m]	Frequency coverage [GHz]	t_{source} [min]
2023.1.00124.S	12-m (C-3)	15–500	85.9–89.9, 97.9–101.9	685
2023.1.00124.S	12-m (C-4)	15–784	85.9–89.9, 97.9–101.9	49
2023.1.00124.S	12-m (C-2)	15–314	85.9–89.9, 97.9–101.9	49
2023.1.00124.S	7-m (ACA)	9–49	85.9–89.9, 97.9–101.9	1616
2022.1.00495.S	12-m (C-3)	15–368	89.1–92.9, 101.1–104.9	198
2022.1.00495.S	12-m (C-2)	15–313	89.1–92.9, 101.1–104.9	148
2017.1.00273.S	12-m (C43-4)	15–784	86.2–89.6, 97.9–101.6	47
2017.1.00273.S	12-m (C43-5)	15–1231	86.2–89.6, 97.9–101.6	116
2017.1.00273.S	12-m (C43-4)	15–784	89.8–93.7, 101.8–105.8	78
2015.1.01543.T	12-m (C40-4)	15–704	84.3–87.9, 96.4–100.0	47

30

Extended Data Table 2 Frequency range of the flagged channels in each tuning.

Program ID	Frequency coverage [GHz]	Flagged channels [GHz]	Flagged fraction
2023.1.00124.S	85.9–89.9, 97.9–101.9	86.5–87.35 (CO), 98.5–98.85 (foreground)	16%
2022.1.00495.S	89.1–92.9, 101.1–104.9	92.4–92.9 ([CI]), 103.1–104.3 (^{13}CO&C^{18}O)	23%
2017.1.00273.S	86.2–89.6, 97.9–101.6	86.5–87.35 (CO), 98.5–98.85 (foreground)	16%
2017.1.00273.S	89.8–93.7, 101.8–105.8	92.4–93.2 ([CI]), 103.1–104.3 (^{13}CO&C^{18}O)	27%
2015.1.01543.T	84.3–87.9, 96.4–100.0	86.5–87.35 (CO), 98.5–98.85 (foreground)	16%

Extended Data Table 3 Details of continuum maps used in this study.

Map	Used data	Frequency coverage [GHz]	uv-range [$k\lambda$]	Taper	$t_{\mathrm{ALMA}} + t_{\mathrm{ACA}}$ [min]	RMS [μJy/beam]	Beam [arcsec^2]	MRS [arcsec]
Deep	all	84.3–93.7, 96.4–105.8	2–400	N/A	1416+1616	1.8	2.4×2.1	33
Deep (tapered)	all	84.3–93.7, 96.4–105.8	2–400	2″	1416+1616	2.1	3.7×3.3	34
ALMA high-res	2023.1.00124.S	85.9–89.9, 97.9–101.9	10–220	N/A	782+0	2.1	2.2×1.9	16
	2017.1.00273.S	86.2–89.6, 97.9–101.6	10–400		163+0			
ALMA low-res	2023.1.00124.S	85.9–89.9, 97.9–101.9	4–10	N/A	782+0	11	14.4×13.4	48
	2017.1.00273.S	86.2–89.6, 97.9–101.6	4–10		163+0			
ACA	2023.1.00124.S	85.9–89.9, 97.9–101.9	2–14	N/A	0+1616	24	18.0×12.1	$\lesssim 76$
SZ	2023.1.00124.S	84.3–87.9, 96.4–100.0	2–10	N/A	782+1616	8.8	13.6×14.7	$\lesssim 72$
	2017.1.00273.S	86.2–89.6, 97.9–101.6	4–10		163+0			

Extended Data Table 4 3-mm continuum source catalog.

ID	R.A. hh:mm:ss	Dec. dd:mm:ss	Distance arcsec	S/N	PB	S_{peak} μJy	S_{kron} μJy	S_{best} μJy	Name[1]
			Distance< 15″ (ALMA high-res)						
1	23:49:43.24	−56:38:30.06	9.0	10.7	0.96	23±2	35±6	35±6	J
2	23:49:43.46	−56:38:26.29	7.2	10.1	0.97	22±2	27±5	27±5	H
3	23:49:42.17	−56:38:26.35	6.5	30.8	0.98	66±2	106±6	106±6	F,I,L
4	23:49:42.78	−56:38:24.49	2.5	89.4	1.00	186±2	286±5	286±5	B,C,G
5	23:49:42.67	−56:38:19.37	2.7	75.2	0.99	158±2	185±5	185±5	A, K
6	23:49:41.21	−56:38:24.73	13.0	25.6	0.90	59±2	64±5	64±5	E
7	23:49:41.41	−56:38:22.49	11.1	44.4	0.92	100±2	107±4	107±4	D
			Total						
ALMA high-res	...	...	...	...	...	614±6	809±14	809±14	
ALMA low-res	23:49:42.36	−56:38:23.79	3.4	45.0	1.00	502±11	678±29	678±29	
ACA	23:49:42.40	−56:38:24.16	3.2	21.8	1.00	515±24	621±40	621±40	
			Distance> 15″ (ALMA high-res)						
8	23:49:38.97	−56:38:57.41	47.2	4.1	0.21	41±10	59±18	59±18	...
9	23:49:40.56	−56:38:06.10	24.1	14.7	0.65	47±3	40±5	47±3	NL1
10	23:49:39.11	−56:37:54.02	41.0	6.6	0.28	49±7	67±18	67±18	...
11	23:49:42.54	−56:37:33.07	49.0	14.0	0.15	197±14	210±23	210±23	N1
Decrement (SZ)	23:49:42.53	−56:38:23.55	2.0	8.4	1.00	−74±9	...	−157±16	

[1]Names of the corresponding protocluster members [See Ref. 11].

Declarations

- **Data availability**: The ALMA and *HST* data used in this work are publicly available on the ALMA science archive (https://almascience.nrao.edu/aq/) and MAST service (https://mast.stsci.edu). The *JWST* data were obtained as a part of program *JWST*-GO-06669, which will be accessible after the proprietary period.
- **Code availability**: Presented results can be reproduced using the following publicly available packages: `astropy` [100], `astroquery` [101], `CASA` [102], `colossus` [78], `matplotlib` [103], `numpy` [104], `pandas` [105], `photutils` [106] `spectral_cube` [107], `uvplot` [108].
- **Author contribution**: D.Z. reduced and analyzed the data, interpreted the results, produced the figures, and drafted the manuscript. S.C.C conceived, designed, and supervised the projects. R.G produced the tSZ model of SPT2349−56 for the ALMA proposal. R.D validated the fidelity of the tSZ decrement. P.A.A calculated the redshift-evolution of the Compton-Y parameter and hot-gas fraction from TNG-Cluster simulations. S.K reduced the JWST NIRCam data. All authors contributed substantially to discussing the results and preparing the manuscript.
- **Author information:** The authors declare no competing interests. Correspondence and requests for materials should be addressed to D.Z. (dzhou.astro@gmail.com).

References

[1] Bryan, G.L., Norman, M.L.: Statistical Properties of X-Ray Clusters: Analytic and Numerical Comparisons. ApJ **495**(1), 80–99 (1998) https://doi.org/10.1086/305262 arXiv:astro-ph/9710107 [astro-ph]

[2] Chiang, Y.-K., Makiya, R., Ménard, B., Komatsu, E.: The Cosmic Thermal History Probed by Sunyaev-Zeldovich Effect Tomography. ApJ **902**(1), 56 (2020) https://doi.org/10.3847/1538-4357/abb403 arXiv:2006.14650 [astro-ph.CO]

[3] Li, Q., Cui, W., Yang, X., Davé, R., Rasia, E., Borgani, S., Massimo, M., Knebe, A., Dolag, K., Sayers, J.: THE THREE HUNDRED Project: the evolution of physical baryon profiles. MNRAS **523**(1), 1228–1246 (2023) https://doi.org/10.1093/mnras/stad1521 arXiv:2305.09629 [astro-ph.GA]

[4] Rohr, E., Pillepich, A., Nelson, D., Ayromlou, M., Péroux, C., Zinger, E.: The cooler past of the intracluster medium in TNG-cluster. MNRAS **536**(2), 1226–1250 (2025) https://doi.org/10.1093/mnras/stae2536 arXiv:2410.19900 [astro-ph.GA]

[5] Sunyaev, R.A., Zeldovich, I.B.: Microwave background radiation as a probe of the contemporary structure and history of the universe. ARA&A **18**, 537–560 (1980) https://doi.org/10.1146/annurev.aa.18.090180.002541

[6] Voit, G.M.: Tracing cosmic evolution with clusters of galaxies. Reviews of Modern Physics **77**(1), 207–258 (2005) https://doi.org/10.1103/RevModPhys.77.207 arXiv:astro-ph/0410173 [astro-ph]

[7] Mroczkowski, T., Nagai, D., Basu, K., Chluba, J., Sayers, J., Adam, R., Churazov, E., Crites, A., Di Mascolo, L., Eckert, D., Macias-Perez, J., Mayet, F., Perotto, L., Pointecouteau, E., Romero, C., Ruppin, F., Scannapieco, E., ZuHone, J.: Astrophysics with the Spatially and Spectrally Resolved Sunyaev-Zeldovich Effects. A Millimetre/Submillimetre Probe of the Warm and Hot Universe. SSRv **215**(1), 17 (2019) https://doi.org/10.1007/s11214-019-0581-2 arXiv:1811.02310 [astro-ph.CO]

[8] Mantz, A.B., Abdulla, Z., Allen, S.W., Carlstrom, J.E., Logan, C.H.A., Marrone, D.P., Maughan, B.J., Willis, J., Pacaud, F., Pierre, M.: The XXL Survey. XVII. X-ray and Sunyaev-Zel'dovich properties of the redshift 2.0 galaxy cluster XLSSC 122. A&A **620**, 2 (2018) https://doi.org/10.1051/0004-6361/201630096 arXiv:1703.08221 [astro-ph.CO]

[9] Gobat, R., Daddi, E., Coogan, R.T., Le Brun, A.M.C., Bournaud, F., Melin, J.-B., Riechers, D.A., Sargent, M., Valentino, F., Hwang, H.S., Finoguenov, A., Strazzullo, V.: Sunyaev-Zel'dovich detection of the galaxy cluster Cl J1449+0856 at z = 1.99: The pressure profile in uv space. A&A **629**, 104 (2019) https://doi.org/10.1051/0004-6361/201935862 arXiv:1907.10985 [astro-ph.CO]

[10] Di Mascolo, L., Saro, A., Mroczkowski, T., Borgani, S., Churazov, E., Rasia, E., Tozzi, P., Dannerbauer, H., Basu, K., Carilli, C.L., Ginolfi, M., Miley, G., Nonino, M., Pannella, M., Pentericci, L., Rizzo, F.: Forming intracluster gas in a galaxy protocluster at a redshift of 2.16. Nature **615**(7954), 809–812 (2023) https://doi.org/10.1038/s41586-023-05761-x arXiv:2303.16226 [astro-ph.CO]

[11] Miller, T.B., Chapman, S.C., Aravena, M., Ashby, M.L.N., Hayward, C.C., Vieira, J.D., Weiß, A., Babul, A., Béthermin, M., Bradford, C.M., Brodwin, M., Carlstrom, J.E., Chen, C.-C., Cunningham, D.J.M., De Breuck, C., Gonzalez, A.H., Greve, T.R., Harnett, J., Hezaveh, Y., Lacaille, K., Litke, K.C., Ma, J., Malkan, M., Marrone, D.P., Morningstar, W., Murphy, E.J., Narayanan, D., Pass, E., Perry, R., Phadke, K.A., Rennehan, D., Rotermund, K.M., Simpson, J., Spilker, J.S., Sreevani, J., Stark, A.A., Strandet, M.L., Strom, A.L.: A massive core for a cluster of galaxies at a redshift of 4.3. Nature **556**(7702), 469–472 (2018) https://doi.org/10.1038/s41586-018-0025-2 arXiv:1804.09231 [astro-ph.GA]

[12] Hill, R., Chapman, S., Scott, D., Apostolovski, Y., Aravena, M., Béthermin, M., Bradford, C.M., Canning, R.E.A., De Breuck, C., Dong, C., Gonzalez, A., Greve, T.R., Hayward, C.C., Hezaveh, Y., Litke, K., Malkan, M., Marrone, D.P., Phadke, K., Reuter, C., Rotermund, K., Spilker, J., Vieira, J.D., Weiß, A.: Megaparsec-scale structure around the protocluster core SPT2349-56 at z = 4.3. MNRAS **495**(3), 3124–3159 (2020) https://doi.org/10.1093/mnras/staa1275 arXiv:2002.11600 [astro-ph.GA]

[13] Chapman, S.C., Hill, R., Aravena, M., Archipley, M., Babul, A., Burgoyne, J., Canning, R.E.A., Deane, R.P., De Breuck, C., Gonzalez, A.H., Hayward, C.C., Kim, S.W., Malkan, M., Marrone, D.P., McIntyre, V., Murphy, E., Pass, E., Perry, R.W., Phadke, K.A., Rennehan, D., Reuter, C., Rotermund, K.M., Scott, D., Seymour, N., Solimano, M., Spilker, J., Stark, A.A., Sulzenauer, N., Tothill, N., Vieira, J.D., Vizgan, D., Wang, G., Weiss, A.: Brightest Cluster Galaxy Formation in the z = 4.3 Protocluster SPT 2349-56: Discovery of a Radio-loud Active Galactic Nucleus. ApJ **961**(1), 120 (2024) https://doi.org/10.3847/1538-4357/ad0b77 arXiv:2301.01375 [astro-ph.GA]

[14] Zhou, D., Chapman, S.C., Sulzenauer, N., Hill, R., Aravena, M., Araya-Araya, P., Cathey, J., Marrone, D.P., Phadke, K.A., Reuter, C., Solimano, M., Spilker, J.S., Vieira, J.D., Vizgan, D., Wang, G.C.P., Weiss, A.: A Large Molecular Gas Reservoir in the Protocluster SPT2349-56 at z = 4.3. ApJL **982**(1), 17 (2025) https://doi.org/10.3847/2041-8213/adb8d8 arXiv:2412.17980 [astro-ph.GA]

[15] Sunyaev, R.A., Zeldovich, Y.B.: Formation of Clusters of Galaxies; Protocluster Fragmentation and Intergalactic Gas Heating. A&A **20**, 189 (1972)

[16] Reuter, C., Vieira, J.D., Spilker, J.S., Weiss, A., Aravena, M., Archipley, M., Béthermin, M., Chapman, S.C., De Breuck, C., Dong, C., Everett, W.B., Fu,

J., Greve, T.R., Hayward, C.C., Hill, R., Hezaveh, Y., Jarugula, S., Litke, K., Malkan, M., Marrone, D.P., Narayanan, D., Phadke, K.A., Stark, A.A., Strandet, M.L.: The Complete Redshift Distribution of Dusty Star-forming Galaxies from the SPT-SZ Survey. ApJ **902**(1), 78 (2020) https://doi.org/10.3847/1538-4357/abb599 arXiv:2006.14060 [astro-ph.GA]

[17] Wang, G.C.P., Hill, R., Chapman, S.C., Weiß, A., Scott, D., Apostolovski, Y., Aravena, M., Archipley, M.A., Béthermin, M., Canning, R.E.A., De Breuck, C., Dong, C., Everett, W.B., Gonzalez, A., Greve, T.R., Hayward, C.C., Hezaveh, Y., Jarugula, S., Marrone, D.P., Phadke, K.A., Reuter, C.A., Rotermund, K.M., Spilker, J.S., Vieira, J.D.: Overdensities of submillimetre-bright sources around candidate protocluster cores selected from the South Pole Telescope survey. MNRAS **508**(3), 3754–3770 (2021) https://doi.org/10.1093/mnras/stab2800 arXiv:2010.02909 [astro-ph.CO]

[18] Tornatore, L., Borgani, S., Springel, V., Matteucci, F., Menci, N., Murante, G.: Cooling and heating the intracluster medium in hydrodynamical simulations. MNRAS **342**(4), 1025–1040 (2003) https://doi.org/10.1046/j.1365-8711.2003.06631.x arXiv:astro-ph/0302575 [astro-ph]

[19] Kravtsov, A.V., Yepes, G.: On the supernova heating of the intergalactic medium. MNRAS **318**(1), 227–238 (2000) https://doi.org/10.1046/j.1365-8711.2000.03771.x arXiv:astro-ph/0004333 [astro-ph]

[20] Conroy, C., Ostriker, J.P.: Thermal Balance in the Intracluster Medium: Is AGN Feedback Necessary? ApJ **681**(1), 151–166 (2008) https://doi.org/10.1086/587861 arXiv:0712.0824 [astro-ph]

[21] McCarthy, I.G., Babul, A., Bower, R.G., Balogh, M.L.: Towards a holistic view of the heating and cooling of the intracluster medium. MNRAS **386**(3), 1309–1331 (2008) https://doi.org/10.1111/j.1365-2966.2008.13141.x arXiv:0706.2768 [astro-ph]

[22] Henden, N.A., Puchwein, E., Sijacki, D.: The redshift evolution of X-ray and Sunyaev-Zel'dovich scaling relations in the FABLE simulations. MNRAS **489**(2), 2439–2470 (2019) https://doi.org/10.1093/mnras/stz2301 arXiv:1905.00013 [astro-ph.CO]

[23] Kooistra, R., Inoue, S., Lee, K.-G., Cen, R., Yoshida, N.: Detecting Preheating in Protoclusters with Lyα Forest Tomography. ApJ **927**(1), 53 (2022) https://doi.org/10.3847/1538-4357/ac4cb1 arXiv:2109.09954 [astro-ph.GA]

[24] Bennett, J.S., Sijacki, D., Costa, T., Laporte, N., Witten, C.: The growth of the gargantuan black holes powering high-redshift quasars and their impact on the formation of early galaxies and protoclusters. MNRAS **527**(1), 1033–1054 (2024) https://doi.org/10.1093/mnras/stad3179 arXiv:2305.11932 [astro-ph.GA]

[25] Dong, C., Lee, K.-G., Ata, M., Horowitz, B., Momose, R.: Observational Evidence for Large-scale Gas Heating in a Galaxy Protocluster at z = 2.30. ApJL **945**(2), 28 (2023) https://doi.org/10.3847/2041-8213/acba89 arXiv:2303.07619 [astro-ph.GA]

[26] Dong, C., Lee, K.-G., Cui, W., Davé, R., Sorini, D.: The effect of AGN feedback on the Lyman-α forest signature of galaxy protoclusters at z 2.3. MNRAS **532**(4), 4876–4888 (2024) https://doi.org/10.1093/mnras/stae1830 arXiv:2402.13568 [astro-ph.GA]

[27] Gardner, A., Baxter, E., Raghunathan, S., Cui, W., Ceverino, D.: Prospects for studying the mass and gas in protoclusters with future CMB observations. The Open Journal of Astrophysics **7**, 2 (2024) https://doi.org/10.21105/astro.2307.15309 arXiv:2307.15309 [astro-ph.CO]

[28] Bigwood, L., Bourne, M.A., Irsic, V., Amon, A., Sijacki, D.: The case for large-scale AGN feedback in galaxy formation simulations: insights from XFABLE. arXiv e-prints, 2501–16983 (2025) https://doi.org/10.48550/arXiv.2501.16983 arXiv:2501.16983 [astro-ph.CO]

[29] Lucie-Smith, L., Peiris, H.V., Pontzen, A., Halder, A., Schaye, J., Schaller, M., Helly, J., McGibbon, R.J., Elbers, W.: Cosmological feedback from a halo assembly perspective. arXiv e-prints, 2505–18258 (2025) arXiv:2505.18258 [astro-ph.CO]

[30] Carlstrom, J.E., Holder, G.P., Reese, E.D.: Cosmology with the Sunyaev-Zel'dovich Effect. ARA&A **40**, 643–680 (2002) https://doi.org/10.1146/annurev.astro.40.060401.093803 arXiv:astro-ph/0208192 [astro-ph]

[31] Spacek, A., Scannapieco, E., Cohen, S., Joshi, B., Mauskopf, P.: Constraining AGN Feedback in Massive Ellipticals with South Pole Telescope Measurements of the Thermal Sunyaev-Zel'dovich Effect. ApJ **819**(2), 128 (2016) https://doi.org/10.3847/0004-637X/819/2/128 arXiv:1601.01330 [astro-ph.GA]

[32] Arnaud, M., Pratt, G.W., Piffaretti, R., Böhringer, H., Croston, J.H., Pointecouteau, E.: The universal galaxy cluster pressure profile from a representative sample of nearby systems (REXCESS) and the Y_{SZ} - M_{500} relation. A&A **517**, 92 (2010) https://doi.org/10.1051/0004-6361/200913416 arXiv:0910.1234 [astro-ph.CO]

[33] Maughan, B.J., Giles, P.A., Randall, S.W., Jones, C., Forman, W.R.: Self-similar scaling and evolution in the galaxy cluster X-ray luminosity-temperature relation. MNRAS **421**(2), 1583–1602 (2012) https://doi.org/10.1111/j.1365-2966.2012.20419.x arXiv:1108.1200 [astro-ph.CO]

[34] Planck Collaboration, Ade, P.A.R., Aghanim, N., Armitage-Caplan, C., Arnaud, M., Ashdown, M., Atrio-Barandela, F., Aumont, J., Baccigalupi, C., Banday,

A.J., Barreiro, R.B., Barrena, R., Bartlett, J.G., Battaner, E., Battye, R., Benabed, K., Benoît, A., Benoit-Lévy, A., Bernard, J.-P., Bersanelli, M., Bielewicz, P., Bikmaev, I., Blanchard, A., Bobin, J., Bock, J.J., Böhringer, H., Bonaldi, A., Bond, J.R., Borrill, J., Bouchet, F.R., Bourdin, H., Bridges, M., Brown, M.L., Bucher, M., Burenin, R., Burigana, C., Butler, R.C., Cardoso, J.-F., Carvalho, P., Catalano, A., Challinor, A., Chamballu, A., Chary, R.-R., Chiang, L.-Y., Chiang, H.C., Chon, G., Christensen, P.R., Church, S., Clements, D.L., Colombi, S., Colombo, L.P.L., Couchot, F., Coulais, A., Crill, B.P., Curto, A., Cuttaia, F., Da Silva, A., Dahle, H., Danese, L., Davies, R.D., Davis, R.J., de Bernardis, P., de Rosa, A., de Zotti, G., Delabrouille, J., Delouis, J.-M., Démoclès, J., Désert, F.-X., Dickinson, C., Diego, J.M., Dolag, K., Dole, H., Donzelli, S., Doré, O., Douspis, M., Dupac, X., Efstathiou, G., Enßlin, T.A., Eriksen, H.K., Finelli, F., Flores-Cacho, I., Forni, O., Frailis, M., Franceschi, E., Fromenteau, S., Galeotta, S., Ganga, K., Génova-Santos, R.T., Giard, M., Giardino, G., Giraud-Héraud, Y., González-Nuevo, J., Górski, K.M., Gratton, S., Gregorio, A., Gruppuso, A., Hansen, F.K., Hanson, D., Harrison, D., Henrot-Versillé, S., Hernández-Monteagudo, C., Herranz, D., Hildebrandt, S.R., Hivon, E., Hobson, M., Holmes, W.A., Hornstrup, A., Hovest, W., Huffenberger, K.M., Hurier, G., Jaffe, T.R., Jaffe, A.H., Jones, W.C., Juvela, M., Keihänen, E., Keskitalo, R., Khamitov, I., Kisner, T.S., Kneissl, R., Knoche, J., Knox, L., Kunz, M., Kurki-Suonio, H., Lagache, G., Lähteenmäki, A., Lamarre, J.-M., Lasenby, A., Laureijs, R.J., Lawrence, C.R., Leahy, J.P., Leonardi, R., León-Tavares, J., Lesgourgues, J., Liddle, A., Liguori, M., Lilje, P.B., Linden-Vørnle, M., López-Caniego, M., Lubin, P.M., Macías-Pérez, J.F., Maffei, B., Maino, D., Mandolesi, N., Marcos-Caballero, A., Maris, M., Marshall, D.J., Martin, P.G., Martínez-González, E., Masi, S., Matarrese, S., Matthai, F., Mazzotta, P., Meinhold, P.R., Melchiorri, A., Melin, J.-B., Mendes, L., Mennella, A., Migliaccio, M., Mitra, S., Miville-Deschênes, M.-A., Moneti, A., Montier, L., Morgante, G., Mortlock, D., Moss, A., Munshi, D., Naselsky, P., Nati, F., Natoli, P., Netterfield, C.B., Nørgaard-Nielsen, H.U., Noviello, F., Novikov, D., Novikov, I., Osborne, S., Oxborrow, C.A., Paci, F., Pagano, L., Pajot, F., Paoletti, D., Partridge, B., Pasian, F., Patanchon, G., Perdereau, O., Perotto, L., Perrotta, F., Piacentini, F., Piat, M., Pierpaoli, E., Pietrobon, D., Plaszczynski, S., Pointecouteau, E., Polenta, G., Ponthieu, N., Popa, L., Poutanen, T., Pratt, G.W., Prézeau, G., Prunet, S., Puget, J.-L.: Planck 2013 results. XX. Cosmology from Sunyaev-Zeldovich cluster counts. A&A **571**, 20 (2014) https://doi.org/10.1051/0004-6361/201321521 arXiv:1303.5080 [astro-ph.CO]

[35] McDonald, M., Allen, S.W., Bayliss, M., Benson, B.A., Bleem, L.E., Brodwin, M., Bulbul, E., Carlstrom, J.E., Forman, W.R., Hlavacek-Larrondo, J., Garmire, G.P., Gaspari, M., Gladders, M.D., Mantz, A.B., Murray, S.S.: The Remarkable Similarity of Massive Galaxy Clusters from z ∼ 0 to z ∼ 1.9. ApJ **843**(1), 28 (2017) https://doi.org/10.3847/1538-4357/aa7740 arXiv:1702.05094 [astro-ph.CO]

[36] Mostoghiu, R., Knebe, A., Cui, W., Pearce, F.R., Yepes, G., Power, C., Dave,

R., Arth, A.: The Three Hundred Project: The evolution of galaxy cluster density profiles. MNRAS **483**(3), 3390–3403 (2019) https://doi.org/10.1093/mnras/sty3306 arXiv:1812.04009 [astro-ph.GA]

[37] Marrone, D.P., Smith, G.P., Okabe, N., Bonamente, M., Carlstrom, J.E., Culverhouse, T.L., Gralla, M., Greer, C.H., Hasler, N., Hawkins, D., Hennessy, R., Joy, M., Lamb, J.W., Leitch, E.M., Martino, R., Mazzotta, P., Miller, A., Mroczkowski, T., Muchovej, S., Plagge, T., Pryke, C., Sanderson, A.J.R., Takada, M., Woody, D., Zhang, Y.: LoCuSS: The Sunyaev-Zel'dovich Effect and Weak-lensing Mass Scaling Relation. ApJ **754**(2), 119 (2012) https://doi.org/10.1088/0004-637X/754/2/119 arXiv:1107.5115 [astro-ph.CO]

[38] Nagarajan, A., Pacaud, F., Sommer, M., Klein, M., Basu, K., Bertoldi, F., Lee, A.T., Ade, P.A.R., Bender, A.N., Ferrusca, D., Halverson, N.W., Horellou, C., Johnson, B.R., Kennedy, J., Kneissl, R., Menten, K.M., Reichardt, C.L., Tucker, C., Westbrook, B.: Weak-lensing mass calibration of the Sunyaev-Zel'dovich effect using APEX-SZ galaxy clusters. MNRAS **488**(2), 1728–1759 (2019) https://doi.org/10.1093/mnras/sty1904 arXiv:1804.03671 [astro-ph.CO]

[39] Bocquet, S., Dietrich, J.P., Schrabback, T., Bleem, L.E., Klein, M., Allen, S.W., Applegate, D.E., Ashby, M.L.N., Bautz, M., Bayliss, M., Benson, B.A., Brodwin, M., Bulbul, E., Canning, R.E.A., Capasso, R., Carlstrom, J.E., Chang, C.L., Chiu, I., Cho, H.-M., Clocchiatti, A., Crawford, T.M., Crites, A.T., de Haan, T., Desai, S., Dobbs, M.A., Foley, R.J., Forman, W.R., Garmire, G.P., George, E.M., Gladders, M.D., Gonzalez, A.H., Grandis, S., Gupta, N., Halverson, N.W., Hlavacek-Larrondo, J., Hoekstra, H., Holder, G.P., Holzapfel, W.L., Hou, Z., Hrubes, J.D., Huang, N., Jones, C., Khullar, G., Knox, L., Kraft, R., Lee, A.T., von der Linden, A., Luong-Van, D., Mantz, A., Marrone, D.P., McDonald, M., McMahon, J.J., Meyer, S.S., Mocanu, L.M., Mohr, J.J., Morris, R.G., Padin, S., Patil, S., Pryke, C., Rapetti, D., Reichardt, C.L., Rest, A., Ruhl, J.E., Saliwanchik, B.R., Saro, A., Sayre, J.T., Schaffer, K.K., Shirokoff, E., Stalder, B., Stanford, S.A., Staniszewski, Z., Stark, A.A., Story, K.T., Strazzullo, V., Stubbs, C.W., Vanderlinde, K., Vieira, J.D., Vikhlinin, A., Williamson, R., Zenteno, A.: Cluster Cosmology Constraints from the 2500 deg^2 SPT-SZ Survey: Inclusion of Weak Gravitational Lensing Data from Magellan and the Hubble Space Telescope. ApJ **878**(1), 55 (2019) https://doi.org/10.3847/1538-4357/ab1f10 arXiv:1812.01679 [astro-ph.CO]

[40] van Marrewijk, J., Di Mascolo, L., Gill, A.S., Battaglia, N., Battistelli, E.S., Bond, J.R., Devlin, M.J., Doze, P., Dunkley, J., Knowles, K., Hincks, A., Hughes, J.P., Hilton, M., Moodley, K., Mroczkowski, T., Naess, S., Partridge, B., Popping, G., Sifón, C., Staggs, S.T., Wollack, E.J.: XLSSC 122 caught in the act of growing up: Spatially resolved SZ observations of a z = 1.98 galaxy cluster. A&A **689**, 41 (2024) https://doi.org/10.1051/0004-6361/202348213 arXiv:2310.06120 [astro-ph.CO]

[41] Andreon, S., Romero, C., Aussel, H., Bhandarkar, T., Devlin, M., Dicker, S., Ladjelate, B., Lowe, I., Mason, B., Mroczkowski, T., Raichoor, A., Sarazin, C., Trinchieri, G.: Witnessing the intracluster medium assembly at the cosmic noon in JKCS 041. MNRAS **522**(3), 4301–4309 (2023) https://doi.org/10.1093/mnras/stad1270 arXiv:2305.02353 [astro-ph.CO]

[42] Bleem, L.E., Stalder, B., de Haan, T., Aird, K.A., Allen, S.W., Applegate, D.E., Ashby, M.L.N., Bautz, M., Bayliss, M., Benson, B.A., Bocquet, S., Brodwin, M., Carlstrom, J.E., Chang, C.L., Chiu, I., Cho, H.M., Clocchiatti, A., Crawford, T.M., Crites, A.T., Desai, S., Dietrich, J.P., Dobbs, M.A., Foley, R.J., Forman, W.R., George, E.M., Gladders, M.D., Gonzalez, A.H., Halverson, N.W., Hennig, C., Hoekstra, H., Holder, G.P., Holzapfel, W.L., Hrubes, J.D., Jones, C., Keisler, R., Knox, L., Lee, A.T., Leitch, E.M., Liu, J., Lueker, M., Luong-Van, D., Mantz, A., Marrone, D.P., McDonald, M., McMahon, J.J., Meyer, S.S., Mocanu, L., Mohr, J.J., Murray, S.S., Padin, S., Pryke, C., Reichardt, C.L., Rest, A., Ruel, J., Ruhl, J.E., Saliwanchik, B.R., Saro, A., Sayre, J.T., Schaffer, K.K., Schrabback, T., Shirokoff, E., Song, J., Spieler, H.G., Stanford, S.A., Staniszewski, Z., Stark, A.A., Story, K.T., Stubbs, C.W., Vanderlinde, K., Vieira, J.D., Vikhlinin, A., Williamson, R., Zahn, O., Zenteno, A.: Galaxy Clusters Discovered via the Sunyaev-Zel'dovich Effect in the 2500-Square-Degree SPT-SZ Survey. ApJS **216**(2), 27 (2015) https://doi.org/10.1088/0067-0049/216/2/27 arXiv:1409.0850 [astro-ph.CO]

[43] Remus, R.-S., Dolag, K., Dannerbauer, H.: The Young and the Wild: What Happens to Protoclusters Forming at Redshift z ≈ 4? ApJ **950**(2), 191 (2023) https://doi.org/10.3847/1538-4357/accb91 arXiv:2208.01053 [astro-ph.CO]

[44] Aljamal, E., Evrard, A.E., Farahi, A., Pillepich, A., Nelson, D., Schaye, J., Schaller, M., Braspenning, J.: Mass Proxy Quality of Massive Halo Properties in the IllustrisTNG and FLAMINGO Simulations: I. Hot Gas (2025). https://arxiv.org/abs/2507.05176

[45] Rotermund, K.M., Chapman, S.C., Phadke, K.A., Hill, R., Pass, E., Aravena, M., Ashby, M.L.N., Babul, A., Béthermin, M., Canning, R., de Breuck, C., Dong, C., Gonzalez, A.H., Hayward, C.C., Jarugula, S., Marrone, D.P., Narayanan, D., Reuter, C., Scott, D., Spilker, J.S., Vieira, J.D., Wang, G., Weiss, A.: Optical and near-infrared observations of the SPT2349-56 proto-cluster core at z = 4.3. MNRAS **502**(2), 1797–1815 (2021) https://doi.org/10.1093/mnras/stab103 arXiv:2006.15345 [astro-ph.GA]

[46] Hlavacek-Larrondo, J., McDonald, M., Benson, B.A., Forman, W.R., Allen, S.W., Bleem, L.E., Ashby, M.L.N., Bocquet, S., Brodwin, M., Dietrich, J.P., Jones, C., Liu, J., Reichardt, C.L., Saliwanchik, B.R., Saro, A., Schrabback, T., Song, J., Stalder, B., Vikhlinin, A., Zenteno, A.: X-Ray Cavities in a Sample of 83 SPT-selected Clusters of Galaxies: Tracing the Evolution of AGN Feedback in Clusters of Galaxies out to z=1.2. ApJ **805**(1), 35 (2015) https:

//doi.org/10.1088/0004-637X/805/1/35 arXiv:1410.0025 [astro-ph.HE]

[47] Valentino, F., Daddi, E., Finoguenov, A., Strazzullo, V., Le Brun, A., Vignali, C., Bournaud, F., Dickinson, M., Renzini, A., Béthermin, M., Zanella, A., Gobat, R., Cimatti, A., Elbaz, D., Onodera, M., Pannella, M., Sargent, M., Arimoto, N., Carollo, M., Starck, J.-L.: A Giant Lyα Nebula in the Core of an X-Ray Cluster at Z = 1.99: Implications for Early Energy Injection. ApJ **829**(1), 53 (2016) https://doi.org/10.3847/0004-637X/829/1/53 arXiv:1605.03194 [astro-ph.GA]

[48] Bassini, L., Rasia, E., Borgani, S., Granato, G.L., Ragone-Figueroa, C., Biffi, V., Ragagnin, A., Dolag, K., Lin, W., Murante, G., Napolitano, N.R., Taffoni, G., Tornatore, L., Wang, Y.: The DIANOGA simulations of galaxy clusters: characterising star formation in protoclusters. A&A **642**, 37 (2020) https://doi.org/10.1051/0004-6361/202038396 arXiv:2006.13951 [astro-ph.GA]

[49] Lim, S., Scott, D., Babul, A., Barnes, D.J., Kay, S.T., McCarthy, I.G., Rennehan, D., Vogelsberger, M.: Is there enough star formation in simulated protoclusters? MNRAS **501**(2), 1803–1822 (2021) https://doi.org/10.1093/mnras/staa3693 arXiv:2010.02259 [astro-ph.GA]

[50] Lim, S., Tacchella, S., Schaye, J., Schaller, M., Helton, J.M., Kugel, R., Maiolino, R.: The FLAMINGO simulation view of cluster progenitors observed in the epoch of reionization with JWST. MNRAS **532**(4), 4551–4569 (2024) https://doi.org/10.1093/mnras/stae1790 arXiv:2402.17819 [astro-ph.GA]

[51] Cielo, S., Babul, A., Antonuccio-Delogu, V., Silk, J., Volonteri, M.: Feedback from reorienting AGN jets. I. Jet-ICM coupling, cavity properties and global energetics. A&A **617**, 58 (2018) https://doi.org/10.1051/0004-6361/201832582

[52] Duan, X., Guo, F.: On the Energy Coupling Efficiency of AGN Outbursts in Galaxy Clusters. ApJ **896**(2), 114 (2020) https://doi.org/10.3847/1538-4357/ab93b3 arXiv:2004.06841 [astro-ph.HE]

[53] Heckman, T.M., Best, P.N.: A Global Inventory of Feedback. Galaxies **11**(1), 21 (2023) https://doi.org/10.3390/galaxies11010021 arXiv:2301.11960 [astro-ph.GA]

[54] Rennehan, D., Babul, A., Moa, B., Davé, R.: The OBSIDIAN model: three regimes of black hole feedback. MNRAS **532**(4), 4793–4809 (2024) https://doi.org/10.1093/mnras/stae1785 arXiv:2309.15898 [astro-ph.GA]

[55] Jennings, F.J., Babul, A., Davé, R., Cui, W., Rennehan, D.: HYENAS: X-ray bubbles and cavities in the intragroup medium. MNRAS **536**(1), 145–165 (2025) https://doi.org/10.1093/mnras/stae2592 arXiv:2407.14415 [astro-ph.GA]

[56] Begelman, M.C., Cioffi, D.F.: Overpressured Cocoons in Extragalactic Radio Sources. ApJL **345**, 21 (1989) https://doi.org/10.1086/185542

[57] Nesvadba, N.P.H., Lehnert, M.D., De Breuck, C., Gilbert, A.M., van Breugel, W.: Evidence for powerful AGN winds at high redshift: dynamics of galactic outflows in radio galaxies during the "Quasar Era". A&A **491**(2), 407–424 (2008) https://doi.org/10.1051/0004-6361:200810346 arXiv:0809.5171 [astro-ph]

[58] Fabian, A.C.: Observational Evidence of Active Galactic Nuclei Feedback. ARA&A **50**, 455–489 (2012) https://doi.org/10.1146/annurev-astro-081811-125521 arXiv:1204.4114 [astro-ph.CO]

[59] Yang, H.-Y.K., Reynolds, C.S.: How AGN Jets Heat the Intracluster Medium—Insights from Hydrodynamic Simulations. ApJ **829**(2), 90 (2016) https://doi.org/10.3847/0004-637X/829/2/90 arXiv:1605.01725 [astro-ph.HE]

[60] Zinger, E., Pillepich, A., Nelson, D., Weinberger, R., Pakmor, R., Springel, V., Hernquist, L., Marinacci, F., Vogelsberger, M.: Ejective and preventative: the IllustrisTNG black hole feedback and its effects on the thermodynamics of the gas within and around galaxies. MNRAS **499**(1), 768–792 (2020) https://doi.org/10.1093/mnras/staa2607 arXiv:2004.06132 [astro-ph.GA]

[61] Martin-Alvarez, S., Iršič, V., Koudmani, S., Bourne, M.A., Bigwood, L., Sijacki, D.: Stirring the cosmic pot: how black hole feedback shapes the matter power spectrum in the FABLE simulations. MNRAS **539**(2), 1738–1755 (2025) https://doi.org/10.1093/mnras/staf470 arXiv:2407.18349 [astro-ph.CO]

[62] Eckert, D., Gastaldello, F., Lovisari, L., McGee, S., Pasini, T., Brienza, M., Kolokythas, K., O'Sullivan, E., Simionescu, A., Sun, M., Ayromlou, M., Bourne, M.A., Chen, Y., Cui, W., Ettori, S., Finoguenov, A., Gozaliasl, G., Kale, R., Mernier, F., Oppenheimer, B.D., Schellenberger, G., Seppi, R., Tempel, E.: Extreme AGN feedback in the fossil galaxy group SDSSTG 4436. arXiv e-prints, 2506–13907 (2025) https://doi.org/10.48550/arXiv.2506.13907 arXiv:2506.13907 [astro-ph.GA]

[63] Sullivan, A., Turner, R.J., Shabala, S.S., Power, C., Young, S.A.: Jet outbursts, non-thermal pressure and the AGN jet duty cycle. arXiv e-prints, 2506–13422 (2025) https://doi.org/10.48550/arXiv.2506.13422 arXiv:2506.13422 [astro-ph.GA]

[64] Chadayammuri, U., Tremmel, M., Nagai, D., Babul, A., Quinn, T.: Fountains and storms: the effects of AGN feedback and mergers on the evolution of the intracluster medium in the ROMULUSC simulation. MNRAS **504**(3), 3922–3937 (2021) https://doi.org/10.1093/mnras/stab1010 arXiv:2001.06532 [astro-ph.GA]

[65] Grayson, S., Scannapieco, E., Davé, R.: Distinguishing Active Galactic Nuclei Feedback Models with the Thermal Sunyaev-Zel'dovich Effect. ApJ **957**(1), 17 (2023) https://doi.org/10.3847/1538-4357/acfd26 arXiv:2310.01502 [astro-ph.GA]

[66] Altamura, E., Kay, S.T., Bower, R.G., Schaller, M., Bahé, Y.M., Schaye, J., Borrow, J., Towler, I.: EAGLE-like simulation models do not solve the entropy core problem in groups and clusters of galaxies. MNRAS **520**(2), 3164–3186 (2023) https://doi.org/10.1093/mnras/stad342 arXiv:2210.09978 [astro-ph.CO]

[67] Guo, F., Oh, S.P.: Feedback heating by cosmic rays in clusters of galaxies. MNRAS **384**(1), 251–266 (2008) https://doi.org/10.1111/j.1365-2966.2007.12692.x arXiv:0706.1274 [astro-ph]

[68] Vogelsberger, M., Marinacci, F., Torrey, P., Genel, S., Springel, V., Weinberger, R., Pakmor, R., Hernquist, L., Naiman, J., Pillepich, A., Nelson, D.: The uniformity and time-invariance of the intra-cluster metal distribution in galaxy clusters from the IllustrisTNG simulations. MNRAS **474**(2), 2073–2093 (2018) https://doi.org/10.1093/mnras/stx2955 arXiv:1707.05318 [astro-ph.CO]

[69] Weinberger, R., Su, K.-Y., Ehlert, K., Pfrommer, C., Hernquist, L., Bryan, G.L., Springel, V., Li, Y., Burkhart, B., Choi, E., Faucher-Giguère, C.-A.: Active galactic nucleus jet feedback in hydrostatic haloes. MNRAS **523**(1), 1104–1125 (2023) https://doi.org/10.1093/mnras/stad1396 arXiv:2211.11771 [astro-ph.GA]

[70] Huško, F., Lacey, C.G., Schaye, J., Nobels, F.S.J., Schaller, M.: Winds versus jets: a comparison between black hole feedback modes in simulations of idealized galaxy groups and clusters. MNRAS **527**(3), 5988–6020 (2024) https://doi.org/10.1093/mnras/stad3548 arXiv:2307.01409 [astro-ph.GA]

[71] Prunier, M., Pillepich, A., Hlavacek-Larrondo, J., Nelson, D.: X-ray cavities in TNG-Cluster: a direct comparison to observations. MNRAS **539**(2), 1040–1064 (2025) https://doi.org/10.1093/mnras/staf525 arXiv:2503.01965 [astro-ph.GA]

[72] Mantz, A.B., Abdulla, Z., Carlstrom, J.E., Greer, C.H., Leitch, E.M., Marrone, D.P., Muchovej, S., Adami, C., Birkinshaw, M., Bremer, M., Clerc, N., Giles, P., Horellou, C., Maughan, B., Pacaud, F., Pierre, M., Willis, J.: The XXL Survey. V. Detection of the Sunyaev-Zel'dovich Effect of the Redshift 1.9 Galaxy Cluster XLSSU J021744.1-034536 with CARMA. ApJ **794**(2), 157 (2014) https://doi.org/10.1088/0004-637X/794/2/157 arXiv:1401.2087 [astro-ph.CO]

[73] Planck Collaboration, Ade, P.A.R., Aghanim, N., Arnaud, M., Ashdown, M., Aumont, J., Baccigalupi, C., Banday, A.J., Barreiro, R.B., Bartlett, J.G., Bartolo, N., Battaner, E., Battye, R., Benabed, K., Benoît, A., Benoit-Lévy, A., Bernard, J.-P., Bersanelli, M., Bielewicz, P., Bock, J.J., Bonaldi, A., Bonavera, L., Bond, J.R., Borrill, J., Bouchet, F.R., Boulanger, F., Bucher, M., Burigana, C., Butler, R.C., Calabrese, E., Cardoso, J.-F., Catalano, A., Challinor, A., Chamballu, A., Chary, R.-R., Chiang, H.C., Chluba, J., Christensen, P.R., Church, S., Clements, D.L., Colombi, S., Colombo, L.P.L., Combet, C., Coulais, A., Crill, B.P., Curto, A., Cuttaia, F., Danese, L., Davies, R.D., Davis, R.J., de Bernardis, P., de Rosa, A., de Zotti, G., Delabrouille, J., Désert, F.-X., Di

Valentino, E., Dickinson, C., Diego, J.M., Dolag, K., Dole, H., Donzelli, S., Doré, O., Douspis, M., Ducout, A., Dunkley, J., Dupac, X., Efstathiou, G., Elsner, F., Enßlin, T.A., Eriksen, H.K., Farhang, M., Fergusson, J., Finelli, F., Forni, O., Frailis, M., Fraisse, A.A., Franceschi, E., Frejsel, A., Galeotta, S., Galli, S., Ganga, K., Gauthier, C., Gerbino, M., Ghosh, T., Giard, M., Giraud-Héraud, Y., Giusarma, E., Gjerløw, E., González-Nuevo, J., Górski, K.M., Gratton, S., Gregorio, A., Gruppuso, A., Gudmundsson, J.E., Hamann, J., Hansen, F.K., Hanson, D., Harrison, D.L., Helou, G., Henrot-Versillé, S., Hernández-Monteagudo, C., Herranz, D., Hildebrandt, S.R., Hivon, E., Hobson, M., Holmes, W.A., Hornstrup, A., Hovest, W., Huang, Z., Huffenberger, K.M., Hurier, G., Jaffe, A.H., Jaffe, T.R., Jones, W.C., Juvela, M., Keihänen, E., Keskitalo, R., Kisner, T.S., Kneissl, R., Knoche, J., Knox, L., Kunz, M., Kurki-Suonio, H., Lagache, G., Lähteenmäki, A., Lamarre, J.-M., Lasenby, A., Lattanzi, M., Lawrence, C.R., Leahy, J.P., Leonardi, R., Lesgourgues, J., Levrier, F., Lewis, A., Liguori, M., Lilje, P.B., Linden-Vørnle, M., López-Caniego, M., Lubin, P.M., Macías-Pérez, J.F., Maggio, G., Maino, D., Mandolesi, N., Mangilli, A., Marchini, A., Maris, M., Martin, P.G., Martinelli, M., Martínez-González, E., Masi, S., Matarrese, S., McGehee, P., Meinhold, P.R., Melchiorri, A., Melin, J.-B., Mendes, L., Mennella, A., Migliaccio, M., Millea, M., Mitra, S., Miville-Deschênes, M.-A., Moneti, A., Montier, L., Morgante, G., Mortlock, D., Moss, A., Munshi, D., Murphy, J.A., Naselsky, P., Nati, F., Natoli, P., Netterfield, C.B., Nørgaard-Nielsen, H.U., Noviello, F., Novikov, D., Novikov, I., Oxborrow, C.A., Paci, F., Pagano, L., Pajot, F., Paladini, R., Paoletti, D., Partridge, B., Pasian, F., Patanchon, G., Pearson, T.J., Perdereau, O., Perotto, L., Perrotta, F., Pettorino, V., Piacentini, F., Piat, M., Pierpaoli, E., Pietrobon, D., Plaszczynski, S., Pointecouteau, E., Polenta, G., Popa, L., Pratt, G.W., Prézeau, G.: Planck 2015 results. XIII. Cosmological parameters. A&A **594**, 13 (2016) https://doi.org/10.1051/0004-6361/201525830 arXiv:1502.01589 [astro-ph.CO]

[74] Remijan, A., Biggs, A., Cortes, P.A., Dent, B., Di Franceso, J., Fomalont, E., Hales, A., Kameno, S., Mason, B., Philips, N., Saini, K., Vila Vilaro, B., Villard, E.: ALMA Technical Handbook,ALMA Doc. 7.3, ver. 1.1. 2019, ALMA Technical Handbook,ALMA Doc. 7.3, ver. 1.1ISBN 978-3-923524-66-2 (2019). https://doi.org/10.5281/zenodo.4511522

[75] Czekala, I., Loomis, R.A., Teague, R., Booth, A.S., Huang, J., Cataldi, G., Ilee, J.D., Law, C.J., Walsh, C., Bosman, A.D., Guzmán, V.V., Le Gal, R., Öberg, K.I., Yamato, Y., Aikawa, Y., Andrews, S.M., Bae, J., Bergin, E.A., Bergner, J.B., Cleeves, L.I., Kurtovic, N.T., Ménard, F., Nomura, H., Pérez, L.M., Qi, C., Schwarz, K.R., Tsukagoshi, T., Waggoner, A.R., Wilner, D.J., Zhang, K.: Molecules with ALMA at Planet-forming Scales (MAPS). II. CLEAN Strategies for Synthesizing Images of Molecular Line Emission in Protoplanetary Disks. ApJS **257**(1), 2 (2021) https://doi.org/10.3847/1538-4365/ac1430 arXiv:2109.06188 [astro-ph.EP]

[76] Fujimoto, S., Ouchi, M., Ono, Y., Shibuya, T., Ishigaki, M., Nagai, H., Momose,

R.: ALMA Census of Faint 1.2 mm Sources Down to ~0.02 mJy: Extragalactic Background Light and Dust-poor, High-z Galaxies. ApJS **222**(1), 1 (2016) https://doi.org/10.3847/0067-0049/222/1/1 arXiv:1505.03523 [astro-ph.GA]

[77] Fujimoto, S., Kohno, K., Ouchi, M., Oguri, M., Kokorev, V., Brammer, G., Sun, F., González-López, J., Bauer, F.E., Caminha, G.B., Hatsukade, B., Richard, J., Smail, I., Tsujita, A., Ueda, Y., Uematsu, R., Zitrin, A., Coe, D., Kneib, J.-P., Postman, M., Umetsu, K., Lagos, C.d.P., Popping, G., Ao, Y., Bradley, L., Caputi, K., Dessauges-Zavadsky, M., Egami, E., Espada, D., Ivison, R.J., Jauzac, M., Knudsen, K.K., Koekemoer, A.M., Magdis, G.E., Mahler, G., Muñoz Arancibia, A.M., Rawle, T., Shimasaku, K., Toft, S., Umehata, H., Valentino, F., Wang, T., Wang, W.-H.: ALMA Lensing Cluster Survey: Deep 1.2 mm Number Counts and Infrared Luminosity Functions at z = 1–8. ApJS **275**(2), 36 (2024) https://doi.org/10.3847/1538-4365/ad5ae2 arXiv:2303.01658 [astro-ph.GA]

[78] Diemer, B.: COLOSSUS: A Python Toolkit for Cosmology, Large-scale Structure, and Dark Matter Halos. ApJS **239**(2), 35 (2018) https://doi.org/10.3847/1538-4365/aaee8c arXiv:1712.04512 [astro-ph.CO]

[79] Diemer, B., Joyce, M.: An Accurate Physical Model for Halo Concentrations. ApJ **871**(2), 168 (2019) https://doi.org/10.3847/1538-4357/aafad6 arXiv:1809.07326 [astro-ph.CO]

[80] Nelson, D., Springel, V., Pillepich, A., Rodriguez-Gomez, V., Torrey, P., Genel, S., Vogelsberger, M., Pakmor, R., Marinacci, F., Weinberger, R., Kelley, L., Lovell, M., Diemer, B., Hernquist, L.: The IllustrisTNG simulations: public data release. Computational Astrophysics and Cosmology **6**(1), 2 (2019) https://doi.org/10.1186/s40668-019-0028-x arXiv:1812.05609 [astro-ph.GA]

[81] Nelson, D., Pillepich, A., Ayromlou, M., Lee, W., Lehle, K., Rohr, E., Truong, N.: Introducing the TNG-Cluster simulation: Overview and the physical properties of the gaseous intracluster medium. A&A **686**, 157 (2024) https://doi.org/10.1051/0004-6361/202348608 arXiv:2311.06338 [astro-ph.GA]

[82] Springel, V.: E pur si muove: Galilean-invariant cosmological hydrodynamical simulations on a moving mesh. MNRAS **401**(2), 791–851 (2010) https://doi.org/10.1111/j.1365-2966.2009.15715.x arXiv:0901.4107 [astro-ph.CO]

[83] Weinberger, R., Springel, V., Pakmor, R.: The AREPO Public Code Release. ApJS **248**(2), 32 (2020) https://doi.org/10.3847/1538-4365/ab908c arXiv:1909.04667 [astro-ph.IM]

[84] Weinberger, R., Springel, V., Hernquist, L., Pillepich, A., Marinacci, F., Pakmor, R., Nelson, D., Genel, S., Vogelsberger, M., Naiman, J., Torrey, P.: Simulating galaxy formation with black hole driven thermal and kinetic feedback. MNRAS **465**(3), 3291–3308 (2017) https://doi.org/10.1093/mnras/stw2944 arXiv:1607.03486 [astro-ph.GA]

[85] Pillepich, A., Springel, V., Nelson, D., Genel, S., Naiman, J., Pakmor, R., Hernquist, L., Torrey, P., Vogelsberger, M., Weinberger, R., Marinacci, F.: Simulating galaxy formation with the IllustrisTNG model. MNRAS **473**(3), 4077–4106 (2018) https://doi.org/10.1093/mnras/stx2656 arXiv:1703.02970 [astro-ph.GA]

[86] Roncarelli, M., Moscardini, L., Borgani, S., Dolag, K.: The Sunyaev-Zel'dovich effects from a cosmological hydrodynamical simulation: large-scale properties and correlation with the soft X-ray signal. MNRAS **378**(4), 1259–1269 (2007) https://doi.org/10.1111/j.1365-2966.2007.11914.x arXiv:astro-ph/0701680 [astro-ph]

[87] Kay, S.T., Peel, M.W., Short, C.J., Thomas, P.A., Young, O.E., Battye, R.A., Liddle, A.R., Pearce, F.R.: Sunyaev-Zel'dovich clusters in Millennium gas simulations. MNRAS **422**(3), 1999–2023 (2012) https://doi.org/10.1111/j.1365-2966.2012.20623.x arXiv:1112.3769 [astro-ph.CO]

[88] McCarthy, I.G., Le Brun, A.M.C., Schaye, J., Holder, G.P.: The thermal Sunyaev-Zel'dovich effect power spectrum in light of Planck. MNRAS **440**(4), 3645–3657 (2014) https://doi.org/10.1093/mnras/stu543 arXiv:1312.5341 [astro-ph.CO]

[89] Vito, F., Brandt, W.N., Comastri, A., Gilli, R., Ivison, R.J., Lanzuisi, G., Lehmer, B.D., Lopez, I.E., Tozzi, P., Vignali, C.: Fast supermassive black hole growth in the SPT2349−56 protocluster at z = 4.3. A&A **689**, 130 (2024) https://doi.org/10.1051/0004-6361/202450225 arXiv:2406.13005 [astro-ph.GA]

[90] Heckman, T.M., Best, P.N.: The Coevolution of Galaxies and Supermassive Black Holes: Insights from Surveys of the Contemporary Universe. ARA&A **52**, 589–660 (2014) https://doi.org/10.1146/annurev-astro-081913-035722 arXiv:1403.4620 [astro-ph.GA]

[91] Nusser, A., Silk, J., Babul, A.: Suppressing cluster cooling flows by self-regulated heating from a spatially distributed population of active galactic nuclei. MNRAS **373**(2), 739–746 (2006) https://doi.org/10.1111/j.1365-2966.2006.11061.x arXiv:astro-ph/0602566 [astro-ph]

[92] Kondapally, R., Best, P.N., Raouf, M., Thomas, N.L., Davé, R., Shabala, S.S., Röttgering, H.J.A., Hardcastle, M.J., Bonato, M., Cochrane, R.K., Małek, K., Morabito, L.K., Prandoni, I., Smith, D.J.B.: Cosmic evolution of radio-AGN feedback: confronting models with data. MNRAS **523**(4), 5292–5305 (2023) https://doi.org/10.1093/mnras/stad1813 arXiv:2306.11795 [astro-ph.GA]

[93] Venkateshwaran, A., Weiss, A., Sulzenauer, N., Menten, K., Aravena, M., Chapman, S.C., Gonzalez, A., Gururajan, G., Hayward, C.C., Hill, R., Reuter, C., Spilker, J.S., Vieira, J.D.: Kinematic analysis of **z = 4.3** galaxies in the SPT2349−56 protocluster core. arXiv e-prints, 2409–13823 (2024) https://doi.org/10.48550/arXiv.2409.13823 arXiv:2409.13823 [astro-ph.GA]

[94] Spilker, J.S., Aravena, M., Phadke, K.A., Béthermin, M., Chapman, S.C., Dong, C., Gonzalez, A.H., Hayward, C.C., Hezaveh, Y.D., Litke, K.C., Malkan, M.A., Marrone, D.P., Narayanan, D., Reuter, C., Vieira, J.D., Weiß, A.: Ubiquitous Molecular Outflows in z ¿ 4 Massive, Dusty Galaxies. II. Momentum-driven Winds Powered by Star Formation in the Early Universe. ApJ **905**(2), 86 (2020) https://doi.org/10.3847/1538-4357/abc4e6 arXiv:2010.12591 [astro-ph.GA]

[95] O'Dea, C.P.: The Compact Steep-Spectrum and Gigahertz Peaked-Spectrum Radio Sources. PASP **110**(747), 493–532 (1998) https://doi.org/10.1086/316162

[96] Yamada, M., Sugiyama, N., Silk, J.: The Sunyaev-Zeldovich Effect by Cocoons of Radio Galaxies. ApJ **522**(1), 66–73 (1999) https://doi.org/10.1086/307604 arXiv:astro-ph/9902069 [astro-ph]

[97] Bromberg, O., Nakar, E., Piran, T., Sari, R.: The Propagation of Relativistic Jets in External Media. ApJ **740**(2), 100 (2011) https://doi.org/10.1088/0004-637X/740/2/100 arXiv:1107.1326 [astro-ph.HE]

[98] Cen, R.: Global preventive feedback of powerful radio jets on galaxy formation. Proceedings of the National Academy of Science **121**(35), 2402435121 (2024) https://doi.org/10.1073/pnas.2402435121 arXiv:2408.12040 [astro-ph.GA]

[99] Boselli, A., Fossati, M., Sun, M.: Ram pressure stripping in high-density environments. A&A Rv **30**(1), 3 (2022) https://doi.org/10.1007/s00159-022-00140-3 arXiv:2109.13614 [astro-ph.GA]

[100] Astropy Collaboration, Price-Whelan, A.M., Lim, P.L., Earl, N., Starkman, N., Bradley, L., Shupe, D.L., Patil, A.A., Corrales, L., Brasseur, C.E., Nöthe, M., Donath, A., Tollerud, E., Morris, B.M., Ginsburg, A., Vaher, E., Weaver, B.A., Tocknell, J., Jamieson, W., van Kerkwijk, M.H., Robitaille, T.P., Merry, B., Bachetti, M., Günther, H.M., Aldcroft, T.L., Alvarado-Montes, J.A., Archibald, A.M., Bódi, A., Bapat, S., Barentsen, G., Bazán, J., Biswas, M., Boquien, M., Burke, D.J., Cara, D., Cara, M., Conroy, K.E., Conseil, S., Craig, M.W., Cross, R.M., Cruz, K.L., D'Eugenio, F., Dencheva, N., Devillepoix, H.A.R., Dietrich, J.P., Eigenbrot, A.D., Erben, T., Ferreira, L., Foreman-Mackey, D., Fox, R., Freij, N., Garg, S., Geda, R., Glattly, L., Gondhalekar, Y., Gordon, K.D., Grant, D., Greenfield, P., Groener, A.M., Guest, S., Gurovich, S., Handberg, R., Hart, A., Hatfield-Dodds, Z., Homeier, D., Hosseinzadeh, G., Jenness, T., Jones, C.K., Joseph, P., Kalmbach, J.B., Karamehmetoglu, E., Kałuszyński, M., Kelley, M.S.P., Kern, N., Kerzendorf, W.E., Koch, E.W., Kulumani, S., Lee, A., Ly, C., Ma, Z., MacBride, C., Maljaars, J.M., Muna, D., Murphy, N.A., Norman, H., O'Steen, R., Oman, K.A., Pacifici, C., Pascual, S., Pascual-Granado, J., Patil, R.R., Perren, G.I., Pickering, T.E., Rastogi, T., Roulston, B.R., Ryan, D.F., Rykoff, E.S., Sabater, J., Sakurikar, P., Salgado, J., Sanghi, A., Saunders, N., Savchenko, V., Schwardt, L., Seifert-Eckert, M., Shih, A.Y.,

Jain, A.S., Shukla, G., Sick, J., Simpson, C., Singanamalla, S., Singer, L.P., Singhal, J., Sinha, M., Sipőcz, B.M., Spitler, L.R., Stansby, D., Streicher, O., Šumak, J., Swinbank, J.D., Taranu, D.S., Tewary, N., Tremblay, G.R., de Val-Borro, M., Van Kooten, S.J., Vasović, Z., Verma, S., de Miranda Cardoso, J.V., Williams, P.K.G., Wilson, T.J., Winkel, B., Wood-Vasey, W.M., Xue, R., Yoachim, P., Zhang, C., Zonca, A., Astropy Project Contributors: The Astropy Project: Sustaining and Growing a Community-oriented Open-source Project and the Latest Major Release (v5.0) of the Core Package. ApJ **935**(2), 167 (2022) https://doi.org/10.3847/1538-4357/ac7c74 arXiv:2206.14220 [astro-ph.IM]

[101] Ginsburg, A., Sipőcz, B.M., Brasseur, C.E., Cowperthwaite, P.S., Craig, M.W., Deil, C., Guillochon, J., Guzman, G., Liedtke, S., Lian Lim, P., Lockhart, K.E., Mommert, M., Morris, B.M., Norman, H., Parikh, M., Persson, M.V., Robitaille, T.P., Segovia, J.-C., Singer, L.P., Tollerud, E.J., de Val-Borro, M., Valtchanov, I., Woillez, J., Astroquery Collaboration, a subset of astropy Collaboration: astroquery: An Astronomical Web-querying Package in Python. AJ **157**(3), 98 (2019) https://doi.org/10.3847/1538-3881/aafc33 arXiv:1901.04520 [astro-ph.IM]

[102] CASA Team, Bean, B., Bhatnagar, S., Castro, S., Donovan Meyer, J., Emonts, B., Garcia, E., Garwood, R., Golap, K., Gonzalez Villalba, J., Harris, P., Hayashi, Y., Hoskins, J., Hsieh, M., Jagannathan, P., Kawasaki, W., Keimpema, A., Kettenis, M., Lopez, J., Marvil, J., Masters, J., McNichols, A., Mehringer, D., Miel, R., Moellenbrock, G., Montesino, F., Nakazato, T., Ott, J., Petry, D., Pokorny, M., Raba, R., Rau, U., Schiebel, D., Schweighart, N., Sekhar, S., Shimada, K., Small, D., Steeb, J.-W., Sugimoto, K., Suoranta, V., Tsutsumi, T., van Bemmel, I.M., Verkouter, M., Wells, A., Xiong, W., Szomoru, A., Griffith, M., Glendenning, B., Kern, J.: CASA, the Common Astronomy Software Applications for Radio Astronomy. PASP **134**(1041), 114501 (2022) https://doi.org/10.1088/1538-3873/ac9642 arXiv:2210.02276 [astro-ph.IM]

[103] Hunter, J.D.: Matplotlib: A 2D Graphics Environment. Computing in Science and Engineering **9**(3), 90–95 (2007) https://doi.org/10.1109/MCSE.2007.55

[104] Harris, C.R., Millman, K.J., Walt, S.J., Gommers, R., Virtanen, P., Cournapeau, D., Wieser, E., Taylor, J., Berg, S., Smith, N.J., Kern, R., Picus, M., Hoyer, S., Kerkwijk, M.H., Brett, M., Haldane, A., Río, J.F., Wiebe, M., Peterson, P., Gérard-Marchant, P., Sheppard, K., Reddy, T., Weckesser, W., Abbasi, H., Gohlke, C., Oliphant, T.E.: Array programming with NumPy. Nature **585**(7825), 357–362 (2020) https://doi.org/10.1038/s41586-020-2649-2

[105] The pandas development Team: pandas-dev/pandas: Pandas. https://doi.org/10.5281/zenodo.3509134

[106] Bradley, L., Sipőcz, B., Robitaille, T., Tollerud, E., Vinícius, Z., Deil, C., Barbary, K., Wilson, T.J., Busko, I., Donath, A., Günther, H.M., Cara, M., Lim, P.L., Meßlinger, S., Conseil, S., Burnett, Z., Bostroem, A., Droettboom, M.,

Bray, E.M., Bratholm, L.A., Ginsburg, A., Jamieson, W., Barentsen, G., Craig, M., Morris, B.M., Perrin, M., Rathi, S., Pascual, S., Georgiev, I.Y.: Astropy-/photutils: 2.0.2. https://doi.org/10.5281/zenodo.13989456 . https://doi.org/10.5281/zenodo.13989456

[107] Ginsburg, A., Koch, E., Robitaille, T., Beaumont, C., Adamginsburg, ZuHone, J., Sipocz, B., Patra, S., Jones, C., Lim, P.L., Rosolowsky, E., Stern, K., Earl, N., De Val-Borro, M., Jrobbfed, Shuokong, Kepley, A., Sokolov, V., Badger, T.G., Maret, S., Garrido, J., Booker, J., Tollerud, E.: radio-astro-tools/spectral-cube: V0.4.4. https://doi.org/10.5281/zenodo.2573901

[108] Tazzari, M.: Mtazzari/uvplot. https://doi.org/10.5281/zenodo.1003113 . https://doi.org/10.5281/zenodo.1003113

49